



HAL
open science

Triassic evaporites: a vast reservoir of brines mobilised successively during rifting and thrusting in the Pyrenees

Michel Cathelineau, Marie-Christine Boiron, Hugo Jakomulski

► To cite this version:

Michel Cathelineau, Marie-Christine Boiron, Hugo Jakomulski. Triassic evaporites: a vast reservoir of brines mobilised successively during rifting and thrusting in the Pyrenees. *Journal of the Geological Society*, In press, pp.jgs2020-259. 10.1144/jgs2020-259 . hal-03262906

HAL Id: hal-03262906

<https://hal.univ-lorraine.fr/hal-03262906>

Submitted on 16 Jun 2021

HAL is a multi-disciplinary open access archive for the deposit and dissemination of scientific research documents, whether they are published or not. The documents may come from teaching and research institutions in France or abroad, or from public or private research centers.

L'archive ouverte pluridisciplinaire **HAL**, est destinée au dépôt et à la diffusion de documents scientifiques de niveau recherche, publiés ou non, émanant des établissements d'enseignement et de recherche français ou étrangers, des laboratoires publics ou privés.

1 **Triassic evaporites: a vast reservoir of brines mobilised successively during rifting and**
2 **thrusting in the Pyrenees**

3 M. Cathelineau*, M.-C. Boiron and H. Jakomulski

4

5

6 **Abstract**

7 Triassic evaporites have a very particular location in the Pyrenees, close to detachment areas
8 between the basement and the sedimentary cover, and constitute enormous chlorine and
9 potentially brine reservoir. During the two successive deformation cycles related
10 successively to the Cretaceous rifting and the convergence during early Cenozoic, brines
11 were expelled and implied in fault activity, breccia formation and fluid-rock interactions.
12 Fluid inclusions from fault infillings and alpine-style fissures sampled all along the Pyrenean
13 chain have a maximal chlorinity close to that of halite-water equilibrium at temperatures
14 between 250 and 350°C. Mixing of brines with low chlorinity waters formed a series of fluids
15 covering an extensive range of salinities. During syn-rift events, the hotter dilute end-
16 member is likely derived from seawater infiltrated and heated near the exhumed mantle as
17 no emerged areas were present at that time. During convergence and thrusting, brines
18 again predominate and mixing occurred with a colder end-member, probably of meteoric
19 origin, consistent with a significant period of relief formation. Brines played, therefore, an
20 essential role in mass and heat transfer during the whole orogenic cycle in the Pyrenees.

21

22 **Other pieces of information**

23

24 Michel Cathelineau

25 Université de Lorraine, CNRS, CREGU, GeoRessources, 54000, Nancy

26

27 Marie-Christine Boiron

28 Université de Lorraine, CNRS, CREGU, GeoRessources, 54000, Nancy

29

30 Hugo Jakomulski

31 Université de Lorraine, CNRS, CREGU, GeoRessources, 54000, Nancy

32

33

34 *Correspondence: michel.cathelineau@univ-lorraine.fr

35

36 Other information

37 **Abbrev. Title: Brine migration, rifting and thrusting in the Pyrenees**

38

39

40

41

42 Keywords: Triassic evaporite, brine, Pyrenees, mantle exhumation, alpine thrusts, fluid
43 inclusions, fluid mixing.

44

45 Salt has often been considered a passive mechanical agent of deformation, favouring nappe
46 displacement thanks to its ductility. Thus, the fundamental characteristic of the salt-forming
47 material is its plasticity, i.e. its ability to flow at low temperatures due to its negligible elastic
48 limit. This creep in the solid-state is linked to the low equivalent viscosity of salt-bearing
49 rocks. In the Pyrenees case, Triassic formations, including clays and evaporitic levels, covered
50 most of the peneplaned Paleozoic basement. A series of works in the '70 to '90s highlighted
51 the role of salt in the pre-alpine deformation, the salt tectonics linked to diapirism
52 (Brinkmann and Logters, 1968; Canérot, 1988; James and Canérot, 1999). Extensional
53 tectonics due to rifting at the end of Cretaceous (Jammes et al., 2009; Tugend et al. 2014;
54 Masini et al., 2014; Teixell et al. 2016; Lagabrielle et al., 2019a and b; Lagabrielle et al. 2020;
55 Labaume and Teixell, 2020) deformed the Mesozoic cover before convergence as fold and
56 thrust belt during Cenozoic. Thus, the last decade emphasised the global geodynamic
57 models of the extension, particularly the rise of the mantle, followed by the Cenozoic
58 compression due to plate movements, and contributed first to putting salt tectonics in the
59 background. Recent works tend, however, to reconsider the role of salt as significant in the
60 local deformation mechanisms at the interfaces between basement rocks and the pile of
61 sedimentary formations in the Mesozoic basins and to propose mixed models (Duretz et al.,
62 2020; Ford and Verges, 2020) as already suggested by Jammes et al. (2009). Pre-rift salt
63 controls the Cretaceous smooth-slopes extensional basins and the subsequent continental
64 rifting mode (Lagabrielle et al. 2020).

65 Although the geodynamic of the Pyrenees was the subject of considerable progress in recent
66 years, there is still one relatively unexplored dimension: the role of interactions between
67 fluids and evaporites in the dynamics of deformation (formation of breccias, fluid-assisted
68 deformation) and the mass and heat transfers. Interactions between evaporites and
69 percolating waters can contribute to transferring certain chemical elements (Na, K, Ca, Mg),
70 and brine-rock interaction could significantly modify the mineralogy of the percolated rock.
71 Dissolution and cementing processes subsequently produce significant changes in the
72 permeability of drains, particularly along fluid pathways. All the above-cited processes can
73 have significant consequences in fluid dynamics (clogging vs dissolution). The detachments
74 are most often located along with the Triassic formations at the interfaces between basins
75 and Hercynian basement. The very particular location of the Triassic series in the vicinity of
76 the décollement zones, whose initial cause is purely sedimentological and issued from the

77 paleogeographic history, becomes then the main factor controlling the deformation style,
78 the nature of the migrating fluids and the overall temperature distribution.

79 Most numerical models of temperature distribution at the crustal-scale do not consider the
80 convection and the role of fluids and admit this shortcoming. However, thermal differences
81 between percolating waters and their host formations can either contribute to heat
82 shallower crustal levels or cool deeper levels along main fluid pathways. Modelling works
83 recognise that this aspect could be essential to consider, but it has not been taken into
84 account so far. However, convection may have occurred in the developing basins and
85 significantly altered the overall thermal regime (Souche et al. 2014). The integration of
86 accurate data obtained on strain-related fluid flow into large-scale geodynamic models
87 would greatly help understand the causes of abnormal heat fluxes and local water-rock
88 interactions along faults.

89 As there is often a large gap between crustal-scale models and very detailed data that are
90 geographically limited to small perimeters, the objective of this study is to compile large-
91 scale data on paleofluids. In this work, a series of fluid salinity on paleofluids were thus
92 obtained for newly formed minerals crystallised in fractures from the Axial Zone (Paleozoic
93 basement) and its Mesozoic cover all along the Pyrenees. These new data obtained on 14
94 localities were then compared to the available data from the literature (16 papers providing
95 data from 29 localities), which are somewhat scattered and heterogeneous, and frequently
96 obtained for other purposes than the description of the fluid geochemistry at the belt scale
97 during the main geodynamic events. The present study tries to define the ranges of
98 chlorinity, the degree of mixing and the style of fluid migration during the two main
99 deformation events which have affected the Pyrenees.

100

101 **Geological context**

102 At the scale of Western Europe, evaporites are widely distributed from Silesia to the Paris
103 Basin, from Aquitaine basin / Biscaye Bay to the south of Iberia (Iberian basin) (Orti et al.,
104 2017). Vast salt basins are also found in North Africa (Leleu et al. 2016; Turner and Sherif,
105 2007; Courel et al., 2003). The Upper Triassic deposits cover the most significant part of the
106 future Pyrenean area (Fig. 1) and have a thickness ranging from 1000 to 2700 m in the
107 Pyrenees and the Aquitaine Basin (Biteau et al. 2006; Orti et al. 2017). Labaume et Teixell
108 (2020) estimate a thickness of 3000 m for the Middle and Upper Triassic using balancing

109 constraints for restoration. There are few other equivalent occurrences of such extreme
110 seawater evaporation over hundreds of kilometres after Trias and extension of evaporites,
111 except Messinian salt deposits and some other Cenozoic basins (Babel and Schreiber, 2014).
112 Thus, thousands of kilometres characterise Keuper salt layers. Triassic formations are
113 deposited onto a peneplaned surface almost flat with some islands after a general erosion,
114 weathering and reddening of the outcropping Variscan terranes. The extension of merged
115 areas at that period has mainly been overestimated in the past. Recent works agree on the
116 extension of Triassic layers and the extension of Mesozoic sediments (Liassic formations and
117 Dogger), particularly in zones now free of Mesozoic sedimentary cover as the French Massif
118 Central or the central part of Pyrenees. Evaporites are intercalated between marls and other
119 siliciclastic sediments. Their thickness is generally significant and may vary between a few
120 meters up to hundreds of meters (Orti et al. 2017) and reach more than 1000 m in the
121 Aquitaine basin (Biteau et al. 2006).

122 The Triassic formations are overlain by a Mesozoic cover whose thickness can reach 3000 m
123 to 4000 m (Teixell et al. 2018; Jammes et al. 2009). The sedimentary cover includes Liassic to
124 Upper Jurassic carbonate platform sediments (Canerot et al., 1978). The syn-rift sediment
125 thickness is locally 5000 m, especially along the Biscaye Bay axis, producing potentially a
126 lithostatic pressure type onto sediments located at the base of the pile, around the
127 transitional depth between hydro- and lithostatic pressures. Evaporites at depth were
128 submitted along the Biscaye rift to more than 6-7 km overlying sediments during the Late
129 Cretaceous, yielding pressures of more than 180 MPa (Duretz et al., 2020).

130 The role of pre-rift salt in Pyrenean deformation was first described in Jammes et al. (2009).
131 Diapirism is controlled by a crustal-scale extension (Nalpas and Brun, 1993) and is initiated
132 by the overburden faults (Vendeville et al., 1995). Based on analogic modelling, Vendeville et
133 al. (1995) consider that thick salt layers cannot transmit the significant differential stresses
134 necessary for basement faults to propagate upward as faults into the overburden. During
135 extreme crustal thinning and mantle exhumation, the pre-rift sediments were mechanically
136 decoupled from the basement either thanks to the Keuper clays or by the salt layers
137 (Canérot et al. 2001, Clerc and Lagabrielle 2014). The presence of such a kind of
138 décollement layer favoured efficient basement-cover decoupling. Once units are decoupled,
139 deformation can develop independently in the cover and the basement with distinct styles,

140 both units being separated by significant distances from their initial position. Large salt
141 diapirs may develop when the décollement thickness increases (Duretz et al., 2020).

142 The early stage of Pyrenean convergence occurred in the Late Cretaceous, with the thrusting
143 of Cretaceous sediments as a pop-up along with the Lakora thrust and North Pyrenean
144 Frontal Thrust (NPFT) (see Fig. 2) in the western Pyrenees (Teixell et al., 2016). A similar
145 deformation style is proposed in the east-central Pyrenees at that time (Mouthereau et al.,
146 2014). Following Teixell (1996), the earliest record of convergence in the vicinity of the two
147 main active thrusts is recorded by the flexural drowning of the Upper Cretaceous shelf
148 limestones in the present-day Axial Zone. The initiation age of “protocollision” is not well
149 defined and could be around 70–75 Ma (Campanian, Mouthereau et al., 2014). During the
150 “protocollision”, the continental crust recovered its pre-rift thickness. Thrusting was
151 accommodated in the basin by a continued slip of the NPFT and the Lakora–Larra thrust,
152 which experienced a significant displacement at that time and is considered a detachment
153 structure.

154 During thrusting, basement rocks close to the unconformity with Trias and Cretaceous units
155 were affected by brittle-ductile deformation. In most cases, earlier shear zones (Hercynian
156 or Jurassic) are reactivated, and new tension gashes are formed (Vissers et al., 2020, for
157 instance, at Cap de Creus). In a series of cases, conjugate fault systems and related
158 secondary open structures are associated with the NNE to ENE shortening direction (at
159 Bielsa, Casas et al., 2003) and tight folds accompanied by subvertical schistosity. The low
160 angle dipping quartz-chlorite-calcite veins attest to the subhorizontal shortening (at Bielsa,
161 Bellahsen et al., 2019). Most available data on thrusts indicate a resetting of Ar-Ar ages of
162 Hercynian micas around 50 Ma, particularly along shear zones indicating a high temperature
163 during the alpine deformation peak. Vacherat et al. (2014) and Bosch et al. (2016) infer the
164 maintenance of high temperatures in the North-Pyrenean Zone before the onset of cooling
165 considered to start after 50 Ma. Thus, the fission-track (FFT) studies indicate that cooling
166 starts after 50 Ma and is enhanced mainly after 35 Ma.

167

168 **Materials**

169 *New sampling and data*

170 A series of representative samples were selected from localities covering all Pyrenees from
171 West to East (Fig. 2). Among these samples, two major types of samples were studied: i)

172 those corresponding to zones of significant water-rock interactions related to syn-rift
173 deformation, ii) those typical of Alpine-style open fractures. The first type is characterised by
174 the development of Mg phyllosilicates (chlorite, talc) in micaschists, dolomitisation in syn-rift
175 carbonate formations and silicification in siliciclastic units (sandstones and quartzites).
176 Several studies consider these water-rock interactions as representative of syn-rift processes
177 and are dated in some instances (albitisation: Poujol et al., 2010, Boulvais et al., 2007; Mg-
178 metasomatism: Boulvais et al., 2006; Boutin et al., 2016; breccias with silicifications and
179 carbonate cements: Debroas et al., (2010), Asti et al., (2019), Incerpi et al., 2020, Nteme
180 Mukonzo et al., 2021, Motte et al., 2021; see later the compilation of available ages). Table 1
181 provides details about localities (host-rock, inferred ages of the formation when available).
182 Figure 3 and 4 show macro-photographs of silicified and dolomitised breccias (Fig. 3A and B)
183 as well as newly formed assemblages in fractures: euhedral quartz and calcite from Col de
184 Jau (Fig. 3C) and quartz crystals, synchronous of talc, formed in cavities from dolostone at
185 Trimouns (Fig. 3D).

186 Sets of open fractures are found in the Paleozoic basement rocks from the axial zone, mostly
187 Devonian marbles or siliciclastic facies, close to shear zones. Open veins are either
188 subhorizontal and compatible with the subhorizontal shortening and therefore considered
189 as alpine-style fissures or correspond to reactivated shear planes. At the kilometre scale,
190 thrusts may be inferred but are now eroded, and the Triassic series are only visible close to
191 the NPF in Ariège and Haute Garonne (Fig. 4A and B). Open cavities filled by euhedral quartz
192 may also develop along former faults or shear zones of varied geometries and in newly
193 formed conjugate fault systems. Euhedral quartz (Fig. 4 C and D) are accompanied by simple
194 mineral assemblages (chlorite-calcite). Chlorite is observed in some instances when Fe-Mg
195 minerals are present in the host rocks, such in granites (Lac d'Estaing area), and some
196 euhedral calcite crystals may develop locally on the quartz prisms.

197 *Literature data:* available data on salinity and homogenisation temperature were taken
198 from the literature to complete the new data set. In the compilation (Table 2), data were
199 made homogeneous in terms of units. Microthermometric data were converted into
200 salinities when no provided, and all expressed in wt.% eq. NaCl. The distribution of localities
201 is given in Fig. 2.

202 Most of the literature data on fluid inclusions considered as synchronous of syn-rift or
203 convergence events based on available geochronological data or geological arguments have

204 been compiled. For a small number of localities, the relation between the available data and
205 the two main events above described is less clear, as the fluid inclusions were studied in
206 older but recrystallised material. Thus, in the case of “old” fault infillings by fluorite, galena
207 or sphalerite deposits, authors consider the earlier mineral assemblages as either Paleozoic
208 or early Mesozoic in age. Such minerals were then deformed and recrystallised later on at
209 unknown periods generally assumed to be Mesozoic (Munoz et al., 2015, Cugerone, 2019).
210 Fanlo et al. (1998) interpret the recrystallisation of fluorite at Parzan as related to the
211 “alpine orogeny” with the expulsion of fluids from sediments during early extensional
212 tectonics, e.g. during rifting, but also consider such fluids as similar to those from the
213 Gavarnie thrust. The similarities between fluid salinity and homogenisation temperatures
214 (Th) of FIs found in these minerals and those related to the rifting/ mantle exhumation stage
215 yield to develop the analogy while remaining cautious on this hypothesis.

216

217 **Methods**

218 In newly studied samples, fluid inclusion assemblages were observed and defined thanks to
219 optical microscopy with an OLYMPUS BX51 (transmitted and reflected light) optical
220 microscope and a VHX-200 KEYENCE numeric microscope.

221 Microthermometry was carried out on fluid inclusions (FI) trapped in quartz overgrowths,
222 quartz cement and druzy quartz in sandstone from the sedimentary cover and quartzite
223 from the basement. It was performed using a Linkam® MDS600 heating-cooling stage,
224 adapted to an Olympus® microscope at the GeoRessources laboratory (Nancy, France). The
225 stage was calibrated with in-house and certified standards by measuring the temperature of
226 the final melting of pure water (0.0 °C) in a silica glass capillary, the triple point of CO₂ in a
227 synthetic FI (-56.6 °C), and the homogenisation temperature (L+V→L) of a natural FI at
228 165°C. The following microthermometric parameters were measured: eutectic temperature
229 (Te), melting temperatures of ice (Tm ice), halite dissolution (Tm NaCl), and homogenisation
230 temperature (L+V→L or L+V+S→L+S; Th). Hydrohalite melting (Tm hh) was not frequently
231 observed. The temperatures of phase changes have a precision of about ± 5 °C for Te, ±0.1
232 °C for Tm ice, and ±1 °C for Tm NaCl and Th.

233 Salinity calculations have been made in the H₂O-NaCl system using data from Bodnar and
234 Vityk (1994) based on Tm ice or Tm halite for fluid inclusions containing halite cube (when

235 Tmh < Th and no Tm hh is available). When both Tm ice and Tm hh or Tm NaCl values were
236 available, salinity was calculated using Steele-MacInnis et al. (2011).

237 The presence of gas components (CO₂, CH₄, N₂) in the fluid inclusions was determined by
238 Raman spectrometry analysis using a DILOR LABRAM Raman spectrometer at the
239 GeoRessources laboratory, University of Lorraine, Nancy, France.

240

241 **Results**

242 ***New data on Fluid Inclusions***

243 *Syn-rift occurrences*

244 Salinity and minimal trapping temperatures (Th) are given in Table 1. In syn-rift metasomatic
245 rocks (Reynès, Col de Jau, Trimouns (new data)), both aqueous FI noted Lw and aqueous FI
246 saturated at room temperature with respect to halite noted Lwh are observed. Salinities
247 range from 27 to 35 wt. % eq. NaCl, with modes from 29 to 30 wt. % eq. NaCl, and Th range
248 from 150 to 247°C, with modes from 160 to 220°C. Traces of gas in FI are found in the
249 different localities, mostly N₂-CO₂ with minor CH₄ (Reynès), CH₄ and N₂ (Jau) and both N₂,
250 CO₂ and CH₄ are present in Trimouns FIs with various gas ratios. These new data confirm the
251 presence of high salinity fluids in Mg-metasomatic zones such as those found at Trimouns
252 (Parseval, 1992, Boiron et al., 2007, Quesnel et al., 2019). Such brines appear as
253 predominant in fault zones in the eastern part of the Pyrenees.

254 *Syn-convergence occurrences*

255 Fluid inclusions in euhedral quartz from syn-convergence tension gashes in the Paleozoic
256 basement rock are two-phase FI with size ranging from 5 to 30 µm, and exceptionally 50 to
257 100 µm (Fig. 5). They are aqueous liquid inclusions (Lw FI), with a vapour phase of about 10-
258 20% and sometimes 25%. FIs in quartz occur either as pseudo-secondary planes, isolated or
259 in small clusters (Fig. 5A, C, E, G) and show in several localities a halite crystal (Lwh FI) (Fig.
260 5B, D, E and F). The relative amount of Lwh inclusions compared to Lw is less than in the syn-
261 rift metasomatic rocks and silicified breccias. Salinities range from 1.2 to 25 wt. % eq. NaCl,
262 with modes from 1.7 to 25 wt. % eq. NaCl. More in detail, at La Calabasse, Coulédous or Val
263 d'Alet, salinities are high, above 20 wt. % eq. NaCl and are limited to a narrow range. At
264 Alzen, Balacet, Vallée d'Aspe (La Cristallère or Portalet), the ranges are also small but values
265 are around 8-10 wt. % eq. NaCl, and 15 wt. % eq. NaCl at St Lary and Estaing. The lowest
266 values (mode at 1.7 wt. % eq. NaCl), lower than seawater salinity, were only recorded at Val

267 d'Aran. Th range from 108 to 235°C, with modes from 110 to 200°C, and up to 230°C at
268 Estaing and Saint Lary. Traces of gas are found, mostly CO₂ with minor CH₄ and N₂ (La
269 Calabasse, St Lary) and a predominance of N₂ in other localities (Val d'Aran, and Val d'Alet,
270 for instance).

271

272 **Literature data**

273 The main features of FIs described in the literature data are compiled in Table 2.

274 *Syn-rift processes*

275 In Chainons Bearnais (Salardon et al., 2016, Corre et al., 2018, Nteme Mukonzo et al., 2021,
276 Motte et al., 2021), salinities of FI in cements synchronous of the rift climax, range from 10
277 to 37 wt. % eq. NaCl, with modes from 14 to 34 wt. % eq. NaCl. Most of the salinity modes
278 are higher than 20 wt. % eq. NaCl. in 90% of the localities. It can be noted that lower salinity
279 fluids (up to 7.5 wt. % eq. NaCl) are observed in dolomites (DC2 to DC3 in Mano formation,
280 Motte et al., 2021) related to early diagenesis. Syn-rift fluids have Th ranges from 130 to
281 280°C, with a few data between 300 and 340°C (dolomite rim, Salardon et al., 2016, syn-rift
282 Dolomite DC4 - Mano, Motte et al., 2021). Th are lower in areas where the sedimentary
283 cover was thinner such as Rouse and Deep Lacq (dolomite in the Mano dolostone at Rouse
284 (Renard et al., 2019) and Deeper Lacq (Bahnan, 2019)). Traces of gas such as CO₂, CH₄, N₂
285 and H₂S were found in most localities in Chainons Bearnais, with variable relative amounts
286 depending on the location.

287 In the Mesozoic cover, north to NPFT, salinities are much lower (mode at 3.5 wt. % eq. NaCl
288 at Rouse (Renard et al., 2019). In Deep Lacq, higher salinities ranging from 8 to 10 eq. wt. %
289 NaCl are due to Triassic fluid inputs (Bahnan, 2019).

290

291 *Syn-convergence processes*

292 In the thrust fault areas, particularly the Gavarnie-Neouvielle area (Banks et al., 1991,
293 McCaig et al., 2000), salinities range from 5 to 34 wt. % eq. NaCl, covering an extensive range
294 of values between these extrema, and Th range from 110 to 230°C. In Monte Perdido
295 (Lacroix et al., 2011), salinities are very low, around 1.6 wt. % eq. NaCl, probably due to the
296 isolation of Ypresian formation from Triassic brines.

297 In the Mesozoic cover, north to NPFT: in Upper Lacq, dolomite and calcite formed from
298 relatively dilute fluids (Bahnan et al., 2020) probably due to the isolation of the upper

299 reservoir and to the proximity from the surface. Alternately Bahnan (2019) describes in the
300 deep Lacq reservoir higher salinity fluids (9-14 wt. % eq. NaCl) during the early convergence
301 stage, as Renard et al. (2019) in syn-convergence fault breccia from Rouse.

302

303 *Reworked ore deposits*

304 Fluid inclusion data from ante-Triassic ore deposits (fluorite and Pb-Zn) in the Central
305 Pyrenees were considered because they are deemed to be affected by later undefined age
306 events sometimes inferred as “Mesozoic” s.l. (Subias and Fernandez-Nieto, 1995; Johnson et
307 al., 1996; Munoz et al. 2015; Cugerone, 2019). In these localities, most salinities are above
308 10 wt. % eq. NaCl, and up to 39 wt. % eq. NaCl. Early quartz at Cierco (Johnson et al., 1996)
309 contains high salinity FIs (28 % eq. NaCl). At Argut and Pal de Rase (Cugerone, 2019) or
310 Portalet (Subias and Fernandez – Nieto, 1995), salinities are lower and range from 1 to 10
311 wt. % eq. NaCl. A 150-280°C Th range was found in most studies at the exception of the
312 Lacore and Argentieres deposits where Th are lower (110-140°C at Les Argentières, up to
313 180°C at Lacore: Munoz et al., 2015).

314

315

316 **General trends**

317 The distribution of all the available data indicates a complete range of salinities between
318 high salinity of Lwh FI, which are saturated with halite at room temperature and low salinity
319 fluids (Fig. 6). In a given sample and locality, the salinity displays in general a narrow range.
320 Th ranges are in some instances indicative of a variety of densities, in particular in the case
321 of Cretaceous occurrences. Such ranges may be attributable to pressure fluctuation, as
322 stretching is limited in quartz and stretched FI carefully discarded.

323

324 **Discussion**

325 ***Mixing between brines and low salinity fluids***

326 Two distinct trends are observed in the Th-salinity diagrams (Fig. 6): i) a trend between an
327 end-member of low salinity close to seawater chlorinity, with Th around 250°C, and an end-
328 member with high salinity, slightly cooler (syn-rift process) (Fig. 6A), ii) a trend between a
329 similar saline end-member than that of the first trend, and a dilute end-member even less
330 saline than seawater, with significantly lower Th than the brine (Fig. 6B). These two trends

331 tend to discriminate a series of localities considered representative of fluid migration during
332 the two distinct main geodynamic stages.

333 The first trend corresponds to the Cretaceous extension with Na (Mg, Ca or Si)
334 metasomatism in basement formation either from the eastern part of the Pyrenees (Reynès,
335 Jau, Trimouns) or western occurrences (Urdach, for instance). Most samples come from
336 locations close to the boundary between the Paleozoic basement and the Mesozoic
337 sedimentary formations, e.g. close to highly deformed remnants of the pre-rift cover,
338 including Triassic units.

339 The second trend (Fig. 6 B) is typically representative of the thrusts, especially the Gavarnie
340 thrust, where Triassic units are pinched in between syn-rift sediments, both being thrust
341 onto the basement. The lower Th of the recharge fluids and the potential low salinity of the
342 end-member could indicate that meteoric fluids are entering the system from above and mix
343 along subvertical or high angle faults, such as proposed for the Néouvielle massif by McCaig
344 et al. (2000).

345 Fig. 6C provides salinity-Th envelopes for reworked ore deposits. High salinities were found
346 in Zn-deposits considered affected by Mesozoic events (Lacore and Les Argentières, Munoz
347 et al., 2015, Crabioules and Victoria, Cugerone, 2019). A series of other localities display
348 similarities with the values found in syn-convergence occurrences (Cierco, Johnson et al.,
349 1996; Tebarray, Lanuza and Portalet, Subias and Frenandez-Nieto, 1995).

350 Figure 7 presents the distribution of salinity per locality in a box plot with range and mode
351 values for the three main categories: reworked ore deposits, syn-rift and syn-convergence
352 (both thrusts and open fractures). The salinity ranges recorded locally in a locality are of two
353 types: i) a salinity whose values are narrowed around a mean value indicating a mixing
354 process elsewhere but not in the trapping zone. Therefore, the mixing product is exported
355 from its production zone and then trapped as a fluid with a homogeneous salinity and, ii)
356 populations of FIs with a wide salinity range indicative of in situ mixing between the two
357 end-members (Fig. 7). In both cases, the saline end-member has all the features of evaporitic
358 brines, equilibrated in temperature with their host formations, particularly chlorinities up to
359 30-35% close to halite saturation at 250-300°C (Fig. 7).

360 At Trimouns, several data agree with the features of the primary evaporitic brines, such as
361 the richness in Na-K-(Mg), Cl isotopes values compatible with evaporated seawater, and a
362 low Cl/Br ratio indicative of evaporated seawater having passed halite saturation, at least for

363 a part of the data (Quesnel et al., 2019). The calcium content is relatively high as in most
364 other similar brines and is generally interpreted as Na-Ca exchange result through brine-rock
365 interactions such as albitisation (McCaig et al., 2000, Boiron et al., 2010). Primary and
366 secondary brines probably mixed as shown by the complete range of Cl/ Br (molar ratio)
367 from 200 above 1000 in syn-rift fluids (Trimouns, Quesnel et al., 2019) and in syn-thrust
368 fluids, 100-250 (at Pic Long and La Glère (Neouvielle Massif) to 1000 - 3000 (at Gistaing and
369 Plan de Larri, close to the Triassic red beds at the unconformity with the basement (McCaig
370 et al., 2000)). At Col d'Etche, close to the Urdach Iherzolite, syn-rift fluids are only secondary
371 brines with Cl/ Br ranging from 2000 to 2320 (Nteme Mukenzo et al., 2021).
372 For the late Cretaceous events linked to rifting, the most probable end-member is seawater
373 as the region was covered mainly by Albian to Cenomanian sea. For the Cenozoic events,
374 brines are diluted by a low salinity end-member with a lower temperature, the mixing
375 producing intermediate salinities down to that of seawater. At Gavarnie, the recharge fluids
376 are interpreted as meteoric waters as the relief permitted to imply such water input as
377 shown by isotopic data (McCaig et al., 2000; Trincal et al., 2017). In sedimentary reservoirs
378 close to the North Pyrenean Frontal Thrust (NFPT) such as Rouse and Deep Lacq, post-rift
379 fluids are still influenced by inputs (Cl, sulfate) from Triassic formations (Renard et al., 2019,
380 Bahnan, 2019).

381

382 ***Predominance of brines at the belt scale***

383 The map from Fig. 8 shows that from west to east, saline fluids are omnipresent at the scale
384 of Pyrenees, all along the axial zone whatever the considered event. There is no specific
385 distribution as brines as the highest salinities are encountered in all parts of the chain.
386 However, localities with the lowest salinities are more frequent north of the North Frontal
387 Pyrenean Thrust (NFPT) in the Cretaceous sedimentary cover, north of the axial zone, and
388 along some thrust zones such as Plan de Lari or Gistain (McCaig et al., 2000). Even low (5-10
389 wt.% eq. NaCl), salinities remain above the seawater salinity for most localities, except at
390 Monte Perdido, where salinity mode is around 1.6 wt.% eq. NaCl (Lacroix et al., 2011).

391 The chlorinity ranges, which indicate mixing between contrasted salinities fluids, are more or
392 less pronounced depending on localities. The most extensive range is reported at Gistain and
393 Parzan (thrusts, McCaig et al. 2000; Fanlo et al. 1998), but also in the Chainons Bearnais at
394 Urdach and Saraille, where processes are attributed to the rifting stage (Salardon et al.,

395 2016, Corre et al. 2018; Nteme Mukonzo et al. 2021). Thus, mixing processes occurred
396 during the two main deformation events.

397 Although most fluids are much above seawater salinities, both Figures 7 and 8 show that the
398 range of salinities cover significantly lower values in material from thrusting zones (in blue in
399 Fig. 7) than in Cretaceous metasomatic zones where most of FI populations include brines
400 with maximal salinities (in red, in Fig. 7). Exceptions are the high salinities found in thrust
401 zones at La Glere and Pic Long and Pic de Port Vieux in zones close to Triassic sediments.
402 Thus, brines flew along thrusting zones, probably escaping from sheared or squeezed Triassic
403 formations, like those found along with the Gavarnie thrust (McCaig et al., 2000). A brine
404 end-member is thus present during the major stages of Alpine thrusting.

405 In syn-convergence fissures from the Paleozoic basement in the Axial zone, FI salinity ranges
406 cover a few weight % eq. NaCl in a given locality, but the data envelopes for all alpine
407 fissures define an alignment superimposed on the series of data already described along
408 main thrust zones such as Gavarnie by McCaig et al. (2000). The whole data set constitutes a
409 nearly continuous trend indicative of varied mixing rates between low and high salinity
410 waters. As the mixing does not occur in fluid trapping, the mixing rate is typical of each
411 locality. As a preliminary conclusion, most alpine fissures formed from saline fluids
412 corresponding to different mixing rates between the saline and dilute end-members. Thus,
413 the Paleozoic basement was penetrated by brines at all scales in the vicinity of significant
414 faults. As fluids display the same features in small fissures or damaged zones as along
415 significant faults and thrusts, migration of brines and dilute fluids can be considered as
416 driven by major pathways, together with a fissure permeability at all scales (tension gashes,
417 joints and faults).

418

419 *The chlorine reservoir*

420 During Upper Triassic, the deposition of clay and salt layers is at the origin of a considerable
421 mass of chlorine as halite covering more than 40000 km² (an approximatively minimal
422 surface for the present-day Pyrenean belt: 400 km long by 100 km large). The shortening has
423 reduced by around 30% the pristine surface of the evaporite. The mean thickness is difficult
424 to estimate: salt layers vary from tens of meters up to 360 m thickness for the Anisian layers
425 (Orti et al., 2017) or even more than 1000 m in the Aquitaine basin. Taking a minimal
426 estimate of 50 m, the pristine surface of evaporites, a minimal estimation of a salt volume

427 of 2600 km³, thus a part of the 50 000 km³ of west European Keuper salt (Evans, 2006, Ryan,
428 2008). The specific location of evaporites at the boundary between the Paleozoic basement
429 and the Mesozoic cover has favoured major detachments. In this process, evaporite layers
430 were squeezed, yielding to the subsequent release of primary brines. Water is present in
431 rock salt as interstitial water and as fluid inclusions (Dubessy et al., 1983, Urai et al., 1986).
432 The amount of primary brines as fluid inclusions or pore fluids within the halite are
433 estimated to reach up 1 to 5 % in volume, as shown by microphotographs in Dubessy et al.
434 (1983). Taking minimal estimates of 1 to 2% of brines in salt layers, the primary brine volume
435 could reach a minimal volume of 26 to 52 km³. Besides, brines in salt play a significant role in
436 the creep of rock salt by pressure-solution (Spiers et al., 1990) and can move in salt under
437 thermal gradients (Shao et al., 2019). Secondary brines issued from halite dissolution can
438 also increase the total brine volume.

439

440 *Triassic chlorine salt source versus serpentinisation salt*

441 The results of this compilation indicate that Triassic evaporites constitute a significant source
442 of chlorine that may have been moved at several periods since Triassic times: first, close to
443 sedimentation periods are at the origin of the local formation of red beds concentrations
444 (Subias et al., 2015); second, during Mesozoic at unknown ages, remobilisation of early
445 metal stock as proposed by Munoz et al.(2015) and Cugerone (2019); third, during the
446 Cretaceous rifting, major convective fluid movements occurred under enhanced thermal
447 gradients produced by the mantle exhumation (Quesnel et al., 2019); fourth, during
448 Cenozoic, fluid displaced along with major thrusts during convergence (McCaig et al., 2000),
449 in particular along sliding zones such as clay and evaporite formations, and their vicinity such
450 as damaged zones. Chlorine is still present at varying concentrations in all thermal waters
451 exploited all along the chain, in localities the most frequently very close to Triassic units
452 pinched along major faults and thrusts. The best examples are located along the NFPT:
453 Salies du Salat near Betchat and Salies du Bearn. Saline thermal waters are also recognised in
454 the area of Eaux Chaudes thrust and close to the NPF around Bagnères de Bigorre (Levet et
455 al., 2002), indicating that remaining chlorine can be still mobilised.

456 For the particular Cretaceous mantle exhumation stage, new concepts have put forward
457 brine formation by interactions between mantle rock and seawater. Hovland et al. (2018)
458 reviewed the different hydrothermal processes which should produce salt and brines

459 through hydrated mineral formation, a mechanism already proposed by several studies
460 (Gleeson et al., 2003, Stober and Bucher, 2004, Richard et al., 2013, Bons et al., 2014, Walter
461 et al., 2016, Martz et al., 2019). Scribano et al. (2017) have suggested that the formation of
462 giant salt deposits should be genetically related to the serpentinisation of ultramafic rocks.
463 Thermodynamic calculation confirms the feasibility of salt formation through the
464 consumption of massive amounts of seawater by serpentine crystallisation at the expense of
465 olivine and a mechanism of salt precipitation by decreasing the hydrothermal solution
466 temperature down to 4°C on the seafloor (Debure et al., 2019). However, this salt formation
467 model does not apply to our deep (more than 3-5 km) systems, where the temperature was
468 maintained around 200-300°C. The brine genesis is feasible in serpentinised mantle rocks
469 and depends on water-rock ratio, temperature, and pCO₂. Alternately, the masses of Triassic
470 and Infra-Lias salt reservoir constitute a huge Cl reservoir able to produce by squeezing
471 significant amounts of potential primary, or through dissolution, secondary brines at the
472 same time as serpentinisation.

473 In the case of Pyrenees, the processes of serpentinisation can mostly be invoked for
474 the rifting stage. Thus, the source of Mg responsible for Mg-metasomatism in silicate rocks
475 and dolomitisation in limestones was frequently attributed to a release of Mg during the
476 serpentinisation process. First of all, serpentinisation is not supposed to release significant
477 amounts of Mg as reactions may be written with conservative Mg. Primary evaporitic brines
478 are also particularly enriched in Mg, which concentration increases continuously with the
479 evaporation rate, the bischofite (MgCl₂·6H₂O) saturation being never reached (Fontes and
480 Matray, 1993). Even in the case of the syn-rift formation of Trimouns Mg-metasomatic halos
481 around 115-100 Ma (Schärer et al., 1999; Boutin et al., 2016), Quesnel et al. (2019)
482 precluded serpentinisation as the main source of chlorine of brines at the origin of talc
483 formation. Thus, most geochemical parameters of brine fluid inclusions, although not
484 incompatible with other processes such as dehydration processes, are close to Triassic
485 evaporated seawater. The low Cl/Br ratios, for instance, below those of seawater, are not
486 explained easily by simple water uptake and necessitate specific Br enrichment processes,
487 such as evaporation after halite saturation. Cl/ Br ratio lower than that of seawater (90 to
488 400), thus after evaporation, were found at Trimouns, but also in the Gavarnie thrust (Banks
489 et al., 1991, McCaig et al., 1995, 2000, Table 2) and other rifts such the Iberian rift from
490 Asturias to the Maestrat basin (Grandia et al., 2003 a and b, Sanchez et al., 2009). Applying

491 Occam's Razor rule, the localisation and abundance of salt along detachment zones where
492 fluids have migrated is such that it is by far the most likely to search the chlorine source
493 there rather than in any other remoted area or process.

494

495 ***P-T conditions of trapping***

496 P-T reconstructions necessitate independent geothermometry as the aqueous fluid
497 inclusions are only characterised by their density and salinity. Trapping occurred at any P-T
498 pair along with FIs representative isochores. Either independent temperature estimates are
499 needed, or hypotheses are required for the geothermal gradients. Two main independent
500 estimates are found in the literature: chlorite geothermometry for some localities and a
501 more comprehensive data set is now available on the organic matter at the scale of the
502 Pyrenees using Raman geothermometry on organic matter (Clerc et al., 2015, Saspiturry et
503 al., 2020) and more detailed zones such as the Chainons Béarnais (Izquierdo-Llaval et al.,
504 2020). The brines related to rift conditions were trapped at Trimouns around 300- 350°C
505 using chlorite thermometry, thermal gradients, and fluid inclusion data (Boiron et al., 2007,
506 Boutin et al., 2016, Quesnel et al., 2019). In Chainons Béarnais, estimates are around 240-
507 280°C at Urdach (FI data, Nteme Mukonzo et al., 2021) and 190-280°C at Sarraillé (FI and
508 chlorite data, Corre et al., 2018). For the thrusts, several indications are provided by chlorite
509 geothermometry (Trincal et al., 2015, 2017) with temperatures around 300 to 350°C, and in
510 exceptional cases above 400°C). Thus, the two main periods of fluid migration occurred
511 within the same temperature range ($300 \pm 60^\circ\text{C}$).

512

513 ***Periods of brine migration in the Pyrenees***

514 Brines are present since the deposition of evaporitic levels. Some authors do not exclude
515 that these brines were responsible during Upper Trias or slightly later for metal transport
516 and deposition in permeable horizons such as sandstones (Subias et al., 2015). Main periods
517 of brine migrations and fluid mixing in the Pyrenees are, however, later, as shown in Figure
518 9, which presents a summary of available ages (water-rock interactions (Na, Ca-Mg
519 metasomatism, deformation (mylonitisation, magmatism, thrusting) for the two considered
520 periods: the Cretaceous mantle exhumation and rifting, and the period of convergence with
521 the pop-up structure of the axial zone. Before mantle exhumation, the temperature close to
522 the boundary between the Palaeozoic basement and the sedimentary cover was a function

523 of the thickness of the deposited post-rift sediments before rifting. There is little evidence of
524 significant brine migration up to the mid-Cretaceous. Exceptions could be localised fluid
525 flows along discontinuities as those described around the 150 Ma event (Cathelineau et al.,
526 2012, Boiron et al., 2010) to the north of the Aquitaine basin, and which have also been
527 described or invoked in the Pyrenees (Boutin et al., 2016, for the chlorite stage dated around
528 160 Ma at Trimounss, Munoz et al., 2015, Cugerone, 2019 for the Pb-Zn occurrence), and
529 Spain (Sanchez et al., 2010). The link between these events, such as those dated at Trimouns
530 (Boutin et al., 2016) and the implication of brines, is not entirely proven.

531 It is difficult to estimate the relative impact of the two deformation stages in reworked ore
532 deposits and when fluids were trapped exactly. However, the salinity-Th pairs of the trapped
533 fluids indicate remarkable similarities with fluids described elsewhere in the present work
534 (Fig. 6). Thus, some fluids have features similar to those of syn-rift occurrences, and others
535 display a better match with syn-convergence localities, as shown in blue in Fig. 6C. Absolute
536 dating would be necessary to ensure these correlations to geodynamic events.

537

538 *Role of salt and brines during the rifting stage*

539 Ages for the rift period and main metasomatism stages range from 120 to 98 Ma (Fig. 9).
540 Both deformation and temperature promoted salt flowing, e. g. diapirism, and reversely the
541 presence of enhanced displacements due to salt plasticity. Salt has an effective viscosity vary
542 from 10^{17} to 10^{20} Pa.s below the equivalent viscosity of other rocks (Carter and Hansen,
543 1983, van Keken et al., 1993) and a density around $2,1 \text{ g/cm}^3$ (Urai et al., 2008) generally
544 below the density of other sediments which are compacted, dehydrated and cemented
545 during diagenesis and burial. When the temperature rises, the salt viscosity decreases
546 according to an exponential law and therefore increases its plasticity. Pressure reduces the
547 salt viscosity and favours its mobility, contrary to other surrounding rocks (carbonates,
548 sandstone, clays), for which diagenesis progressively increases the viscosity. Besides, salt
549 contains water which weakens its mechanical properties (Urai et al., 2008) and participates
550 in pressure solution governing creep (Spiers et al., 1990). The peculiar properties of salt
551 explain the halotectonics and the prominent role of salt in the Pyrenean tectonic evolution.
552 It can be noted that the presence of water lowers the viscosity of the salt and allows it to
553 behave like a quasi-Newtonian fluid. Therefore, brines present at the grain boundaries
554 within the evaporites enhance the deformation of the evaporite formations.

555 Temperature affects the rheology of saline rocks by lowering the viscosity of salt. In the
556 Pyrenees, the significant increase of temperature due to mantle uplift yields to halite
557 flowing. Thus, heat and temperature gradients substantially affect a thick layer of salt
558 (Jackson and Talbot, 1986) and favour gravity instability and subsequent diapirism (Fig. 10 A,
559 B). Therefore, it is logical that the first stage of diapirism and salt tectonics occurred during
560 the Cretaceous rifting period of increased thermal gradients. The importance of crustal
561 extension in diapirism initiation was thus recognised in the Pyrenees (Brinkmann and
562 Logters, 1968; Masini et al., 2014; Duretz et al., 2020). Together with the temperature effect,
563 the tectonic regime during pre- and syn-rift stages had also significant consequences on the
564 localisation of salt flows (Canerot et al., 2005). The early history of rifts is mainly put
565 forward, especially the extension of the pre-rift deposits during mid-Cretaceous rifting, or
566 even during Jurassic, with an early salt mobilisation in relation with basement faulting,
567 followed by later gliding of evaporites during the rift climax (Labaume and Teixell, 2020).

568 Brines were trapped at relatively high temperatures between 250°C and 350°C at Trimouns
569 and Urdach, taking trapping temperatures (T_h corrected from pressure). Main salinity- T_h
570 trends from Fig. 6 underline the similarity of the salinity- T_h pairs of the hypersaline fluids
571 and the mixing trend between these brines and a hotter dilute end-member, inferred as
572 seawater. Waters entering in contact with the denudated mantle just above the rift axis
573 during the rifting stage could have undergone overheating. Heated seawater could have
574 brought heat when coming from abnormal temperature areas (Fig. 10B and C). Laterally,
575 strong temperature gradients favoured fluid convection, major fluid pathways being the
576 decollement planes. The venue of these hot waters along the sliding planes of the Triassic
577 units and their mixing with brines may have triggered water-rock interactions and facilitated
578 movements on the planes of detachment. At the end of the rifting process, upper
579 Cretaceous sediments could have acted as fluid barriers and may explain that brines become
580 the predominant fluids again, as seawater do not enter anymore in the system (Fig. 10D and
581 E). Such a process was inferred in the case of the late silicification at Urdach: mixing trends
582 between saline and dilute end-members are typical of the early silicification, and during later
583 stages, quartz cement formed from hypersaline brine suggesting that the unconformity was
584 isolated due to the deposition of the Cenomanian flysch, limiting or stopping the venue of
585 seawater (Nteme Mukonzo et al., 2021).

586

587 *Brines and salt during the convergence stage*

588 The remaining halite bearing formations, when not entirely dislocated during the rifting
589 stage, and the diapiric structures have been rejuvenated and reactivated during shortening.
590 For instance, squeezing and welding of the diapiric zone from the upper European margin
591 formed the NPFT (Labaume and Teixell, 2020). Thus, thrusting benefited from the peculiar
592 rheological properties of Triassic evaporite/clay levels. The beginning of convergence (proto-
593 collision following Vacherat et al., 2014) is proposed around 84 Ma (Labaume and Teixell,
594 2020), with subduction of a thin crustal domain (Mouthereau et al., 2014). Thrusting is dated
595 around 45-35 Ma in the Gavarnie region (38 Ma for the Eaux Chaudes, 33,5 Ma for Gavarnie
596 thrust (Rahl et al., 2011), younger ages in the Spanish part (33-20 Ma), synthesis in Labaume
597 et al., 2016), and to the east of the Pyrenees around 42-49 Ma along with the Pedraforca
598 thrust (Cruset et al., 2020) (Fig. 9). The period of brine migration during thrusting is,
599 therefore, shorter than during the Cretaceous rifting.

600 Along thrust faults, fluids interact with Triassic evaporites as suggested by strontium isotopic
601 data (for instance, Cruset et al., 2020 at Pedraforca). Meteoric waters during their
602 downward migration from highs are probably in thermal disequilibrium and consequently
603 cool the fault damaged zone (Fig. 11). The anisothermal mixing between hot brines with
604 shallower and cooler fluids occur when faults and major thrusts bring the two fluid end-
605 members in contact.

606 Schema from Fig. 11 A emphasises the potential fluid pathways of Triassic brines all along
607 with the thrusts and their mixing with meteoric waters, downward infiltrated from highs.
608 Away from the main thrusting planes, fluids may also mix in brittle structure networks and
609 damaged zones around faults such as in the Néouvielle massif. In such a model, meteoric
610 waters are cooler than brines issued from more profound levels. The mixing is thus
611 anisothermal and explains the generalised trend from Fig. 6B. In the Ariège area (Fig. 11B),
612 below the overlying thrust zones now eroded, fluids infiltrate vertically, thanks to the
613 subvertical structures in the Paleozoic basement, and precipitate quartz in tension gashes
614 close to active shear faults (Fig. 11C).

615 Convergence is followed by a period of quick exhumation between 35 and 25 Ma,
616 synchronous of the collision cessation (Mouthereau et al., 2014), with subsequent cooling
617 (Fillon et al., 2021) and easier penetration of surface waters. During the post-orogenic

618 exhumation phase and up to the present day, meteoric inputs are predominant (saline
619 thermal waters).

620

621

622 **Conclusions**

623 The main conclusions are as follows:

- 624 - During Upper Triassic, the deposition of clay and salt layers is at the origin of a huge
625 mass of chlorine as halite covering more than 40000 km². Using a minimal value of
626 50 m thickness, the estimated salt volume is 2600 km³. The specific location of
627 evaporites at the boundary between the Paleozoic basement and the Mesozoic cover
628 has undoubtedly played a major role in forming the detachments. In this process,
629 evaporite layers were squeezed, leading to the subsequent release of primary brines.
630 The pristine volume of primary brines as fluid inclusions and interstitial fluids could
631 have reached a few tens of km³.
- 632 - During rifting stages, the very particular location of the Triassic evaporites in the
633 vicinity of the décollement zones yielded Triassic formation played a prominent role
634 in detachment zones where the upper crust basement was in contact with both the
635 exhumed mantle and the pre-rift sedimentary cover. Primary brines were primarily
636 expelled during extension and then relayed by secondary brines produced by
637 evaporite dissolution by seawater. Their mixing produced a series of fluids with a
638 chlorinity covering a vast range from 35 to 5 wt. % eq. NaCl.
- 639 - During convergence, evaporitic layers played a mechanical role, particularly well
640 exposed along the Gavarnie thrust. Meteoric waters were implied in the mixing
641 processes during convergence. Production and migration of fluids occur from Triassic
642 times to the end of Cenozoic, therefore for a much more extended period than that
643 the potential formation of brines by mantle rock-water interactions, such as
644 serpentinisation.
- 645 - Consequently, the debate about the respective roles of Triassic brines and mantle-
646 seawater interactions derived brines concerns a relatively short period compared to
647 the rather long period of movements recorded for the Triassic brine migrations.
648 Suppose the dewatering could be the cause of chlorinity increase of fluids entering
649 mantle rocks during the late Cretaceous, it could be, therefore, a further cause of

650 chlorinity increase. The substantial initial chlorine reservoir remains, however,
651 undoubtedly the most significant contribution to the occurrence of brines circulating
652 during a long-lasting period in the Pyrenees.

653 - As a whole, the evaporitic Triassic series played a role in all stages of the Pyrenees
654 evolution. The most remarkable feature of fluids in motion by the several
655 geodynamic episodes is their high salinity, a significant part being close to
656 equilibrium with halite. The other part is a product of partial mixing with waters
657 entering from upper levels.

658 - Although separated by 50-70 Ma, the two deformation events (syn-rift extension and
659 thrusting) are characterised by a similar fluid mixing pattern involving the same salt
660 end member. During both events, the temperature conditions are identical ($300 \pm$
661 60°C), raising the question of temperature evolution between the two events and the
662 existence of relatively high gradients over a reasonably long period.

663 - In the deposits considered ante-Triassic in the Axial zone, fluid inclusions display very
664 similar salinity and density to those described in the syn-rift and syn-convergence
665 fractures. Despite the absence of absolute dates, this analogy suggests that the
666 fluids at the origin of the remobilisations correspond to one of the two main events
667 that affected the Pyrenees.

668

669 **Acknowledgements**

670 Work on Pyrenean paleofluids has been initiated for many years thanks to the collaboration
671 with colleagues from Geosciences Rennes (P. Boulvais, Y. Lagabriele) and benefited from
672 recent discussions with Y. Lagabriele at the occasion of the study of Urdach fluids. New data
673 presented here are issued from a Licence stay of Hugo Jakomulski realised in 2017-2018 at
674 GeoRessources. The data compilation, carried out in late 2020, has been besides stimulated
675 during the simultaneous scientific program "Fluids" by TOTAL and discussions with E.
676 Gaucher and S. Calassou in the preceding years, as well as B. Quesnel during his post-
677 doctoral research at CREGU on Mg-metasomatism. F. Ferracin is thanked for providing
678 excellent material from Ariège quartz-filled fractures and observations. Mar Moragas and
679 David Banks are warmly acknowledged for their constructive and valuable reviews and
680 Giovanni Camanni for editorial handling.

681

682 **Author contributions**

683 **MC:** conceptualization (lead), interpretation, writing

684 **MCB:** conceptualisation (supporting), data reduction and synthesis

685 **HJ:** petrography and microthermometry on fluid inclusions

686

687

688

689 **References**

690

691 Asti, R., Lagabrielle, Y., Fourcade, S., Corre, B. and Monié, P. 2019. How do continents
692 deform during mantle exhumation? Insights from the northern Iberia inverted paleo-passive
693 margin, western Pyrenees (France). *Tectonics* **38**, 1666–1693. DOI: 10.1029/2018TC005428.

694

695 Babel, M. and Schreiber, B. 2014. Geochemistry of Evaporites and Evolution of Seawater,
696 Treatise on Geochemistry. Elsevier, **9.17**, 483-560. DOI: 10.1016/B978-0-08-095975-7.00718-
697 X

698

699 Bahnan A.E., 2019. Fluid circulation and diagenesis of the Lacq Petroleum System: Impact of
700 the geodynamic evolution. PhD thesis, Univ of Lorraine, 218 p.

701

702 Bahnan, A.E., Carpentier, C., Pironon, J., Ford M., Ducoux, M., Barré, G., Mangenot, X. and
703 Gaucher E.C. 2020. Impact of geodynamics on fluid circulation and diagenesis of carbonate
704 reservoirs in a foreland basin: Example of the Upper Lacq reservoir Aquitaine basin, SW
705 France). *Marine Petroleum. Geology*, **111**, 676-694.

706

707 Banks, D.A., Davies, G.R., Yardley, B.W.D., McCaig, A.M. and Grant, N.T. 1991. The chemistry
708 of brines from an Alpine thrust system in the Central Pyrenees: an application of fluid
709 inclusion analysis to the study of fluid behaviour in orogenesis. *Geochimica Cosmochimica*
710 *Acta*, **55**, 1021-1030

711

712 Bellahsen, N., Bayet, L., Denele, Y., Waldner, M., Airaghi, L., Rosenberg, C., Dubacq, B.,
713 Mouthereau, F., Bernet, M., Pik, R., Lahfid, A. and Vacherat, A. 2019. Shortening of the axial
714 zone, Pyrenees: Shortening sequence, upper crustal mylonites and crustal strength.
715 *Tectonophysics*, **766**, 433-452.

716

717 Biteau, J.J., Le Marrec, A., Le Vot, M. and Masset, J.M. 2006. The Aquitaine Basin. *Petroleum*
718 *Geoscience*, **12**, 247–273. DOI: 10.1144/1354-079305-674.

719

720 Bodnar, R.J. and Vityk, M.O. 1994. Interpretation of microthermometric data for H₂O-NaCl
721 fluid inclusions. In: Fluid Inclusions in Minerals, Methods and Applications, B. De Vivo and M.
722 L. Frezzotti, eds, pub. Virginia Tech, Blacksburg, 117–130.

723

724 Boiron, M.C., Cathelineau, M., Dubessy, J., Fabre, C., Boulvais, P. and Banks, D.A. 2007. Na-
725 Ca-Mg rich brines and talc formation in the giant talc deposit of Trimouns (Pyrenees): fluid
726 inclusion chemistry and stable isotope study. European Current Research on Fluid Inclusions,
727 Bern, p. 90.

728

729 Boiron, M.C., Cathelineau, M. and Richard A. 2010. Fluid flows and metal deposition near
730 basement/cover unconformity: Lessons and analogies from Pb-Zn-F-Ba systems for the
731 understanding of Proterozoic U deposits. *Geofluids*, **10**, 270-292.

732

733 Bons, P., Fusswinkel, T., Gomez-Rivas, E., Markl, G., Wagner, T. and Walter, B. 2014. Fluid
734 mixing from below in unconformity-related hydrothermal ore deposits. *Geology*, **42**, 1035-
735 1038.

736

737 Bosch, G.V., Teixell, A., Jolivet, M., Labaume, P., Stockli, D., Domenech, M., and Monié, P.
738 2016. Record of Eocene-Miocene thrusting in the western Axial Zone and Chaînons Béarnais
739 (west-central Pyrenees) revealed by multi-method thermochronology. *Comptes Rendus.*
740 *Geosciences*, **348**, 246-256.

741

742 Boulvais, P., de Parseval, P., D’Hulst, A. and Paris, P. 2006. Carbonate alteration associated
743 with talc-chlorite mineralisation in the eastern Pyrenees, with emphasis on the St.
744 Barthelemy Massif. *Mineralogy Petrology*, **88**, 499–526.

745

746 Boulvais, P., Ruffet, G., Cornichet, J. and Mermet, M. 2007. Cretaceous albitization and
747 dequartzification of Hercynian peraluminous granite in the Salvezines Massif (French
748 Pyrénées). *Lithos*, **93**, 89–106.

749

750 Boutin, A., de Saint Blanquat, M., Poujol, M., Boulvais, P., de Parseval, P., Rouleau, C., and
751 Robert, J.F. 2016. Succession of Permian and Mesozoic metasomatic events in the Eastern

752 Pyrenees with emphasis on the Trimouns talc-chlorite deposit. *International Journal of Earth*
753 *Sciences*, **105**, 747–770.

754

755 Brinkmann, R. and Logters, H. 1968. Diapirs in Western Pyrenees and Fore-land Spain. In:
756 Diapirism and Diapirs: A symposium (Ed. by BRAUNSTEIN J. and O'Brien. G.). *American*
757 *Association Petroleum Geology*, **8**, 275-292.

758

759 Canals, A., Cardellach, E., Moritz, R. and Soler, A. 1999. The influence of enclosing rock type
760 on barite deposits, eastern Pyrenees, Spain: Fluid inclusion and isotope (Sr, S, O, C) data.
761 *Mineralium Deposita*, **34**, 199-210.

762

763 Canérot, J. 1988. Manifestations de l'halocinèse dans les chaînons béarnais (Zone Nord-
764 Pyrénéenne) au Crétacé inférieur. *Comptes-Rendus Académie Sciences*, **306**, 1099–1102.

765

766 Canérot, J., Peybernes, B. and Cizsak, R. 1978. Présence d'une marge méridionale à
767 l'emplacement des Chaînons Béarnais (Pyrénées basco-béarnaises). *Bulletin Société*
768 *Géologique de France*, **7(20)**, 673–676.

769

770 Canérot, J., Majesté-Menjoulas, C. and Ternet, Y. 2001. La faille Nord- Pyrénéenne, mythe ou
771 réalité ? Le couloir de décrochement de Bielle–Accous, élément de réponse du terrain en
772 Aspe et Ossau (Pyrénées-Atlantiques). *Strata*, **2-37**, 1–36.

773

774 Canérot, J., Hudec, M.R. and Rockenbauch, K. 2005. Mesozoic diapirism in the Pyrenean
775 orogen: Salt tectonics on a transform plate boundary, *AAPG Bulletin*, **89**, 211–229,
776 <https://doi.org/10.1306/09170404007>

777

778 Carter, N.L. and Hansen, F.D. 1983). Creep of rocksalt. *Tectonophysics*, **92**, 275-333.

779

780 Casas, A.M., Oliva, B., Roman-Berdiel, T. and Pueyo E. 2003. Basement deformation: Tertiary
781 folding and fracturing of the Variscan Bielsa granite (Axial Zone, central Pyrenees),
782 *Geodynamica Acta*, **16**, 99–117.

783

784 Cathelineau, M., Boiron, M.C., Fourcade, S., Ruffet, G., Clauer, N., Belcourt, O., Coulibaly, Y.,
785 Banks, D.A. and Guillocheau, F. 2012. A major Late Jurassic fluid event at the
786 basin/basement unconformity in western France: $^{40}\text{Ar}/^{39}\text{Ar}$ and K–Ar dating, fluid
787 chemistry, and related geodynamic context. *Chemical Geology*, **322–323**, 99–120.
788

789 Clerc, C. and Lagabriele, Y. 2014. Thermal control on the modes of crustal thinning leading
790 to mantle exhumation: Insights from the Cretaceous Pyrenean hot paleomargins. *Tectonics*,
791 **33**, 1340–1359.
792

793 Clerc, C., Lahfid, A., Monié, P., Lagabriele, Y., Chopin, C., Poujol, M., Boulvais, P.,
794 Ringenbach, J.-C., Masini, E. and de St Blanquat, M. 2015. High-temperature metamorphism
795 during extreme thinning of the continental crust: a reappraisal of the North Pyrenean
796 passive paleomargin. *Solid Earth*, **6**, 643–668.
797

798 Corre, B., Boulvais, P., Boiron, M.C., Lagabriele, Y., Marasi, L. and Clerc, C. 2018. Fluid
799 circulations in response to mantle exhumation at the passive margin setting in the north
800 Pyrenean zone, France. *Mineralogy Petrology*, **97**, 109-142. DOI: 10.1007/s00710-018-0559-
801 x.
802

803 Courel, L., Ait Salem, H., Benaouiss, N., Et-Touhami, M., Fekirine, B., Oujjidi, M., Soussi, M.
804 and Tourani, A. 2003. Mid-Triassic to Early Liassic clastic/evaporitic deposits over the
805 Maghreb platform. *Paleogeography, Paleoclimatology, Paleoecology*, **196**, 157-176.
806

807 Cruset, D., Cantarero, I., Benedicto, A., John, C. M., Vergés, J., Albert, R., Gerdes, A. and
808 Travé, A. (2020). From hydroplastic to brittle deformation: controls on fluid flow in fold and
809 thrust belts. Insights from the Lower Pedraforca thrust sheet (SE Pyrenees), *Marine*
810 *Petroleum Geology*, **120**, 104517. doi.org/10.1016/j.marpetgeo.2020.104517
811

812 Cugerone, A. 2019. Impact of recrystallisation and metamorphism on the mobility of
813 germanium and related elements in orogenic Pb-Zn deposits: example of the Pyrenean Axial
814 Zone mineralisations (France-Spain). PhD thesis, University of Montpellier, HAL Id: tel-
815 02578708

816
817 Debroas, E.J., Canérot, J. and Bilotte, M. 2010. Les Brèches d’Urdach, témoins de
818 l’exhumation du manteau pyrénéen dans un escarpement de faille Vraconnien-Cénomani
819 inférieur (zone nord-pyrénéenne, Pyrénées-Atlantiques, France). *Géologie de la France*, **2**,
820 53–63.

821
822 Debure, M., Lassin, A., Marty, N.C., Claret, F., Virgone, A., Calassou, S. and Gaucher, E.C.
823 2019. Thermodynamic evidence of giant salt deposit formation by serpentinitisation: an
824 alternative mechanism to solar evaporation. *Scientific reports*, **9**, 1-11.

825
826 Dubessy, J., Geisler, D., Kosztolanyi, C. and Vernet, M. 1983. The determination of sulphate
827 in fluid inclusions using the M.O.L.E. Raman microprobe. Application to a Keuper halite and
828 geochemical consequences. *Geochimica Cosmochimica Acta*, **47**, 1-10.

829
830 Duretz, T., Asti, R., Lagabrielle, Y., Brun, J.P., Jourdon, A., Clerc, C. and Corre, B. 2020.
831 Numerical modelling of syn-rift salt tectonics and mantle exhumation in the Cretaceous
832 Pyrenean Rift. *Basinal Research*, doi.org/10.1111/bre.12389

833
834 Evans, D. A. D. 2006. Proterozoic low orbital obliquity and axial-dipolar geomagnetic field
835 from evaporite palaeolatitudes. *Nature*, **444**, 51–55.

836
837 Fallourd, S., M. Poujol, P. Boulvais, J.-L. Paquette, M. de Saint Blanquat, and P. Rémy 2014. In
838 Situ LA-ICP-MS U–Pb Titanite Dating of Na–Ca Metasomatism in Orogenic Belts: The North
839 Pyrenean Example. *International Journal of Earth Sciences*, **103**, 667–682,
840 doi.org/10.1007/s00531-013-0978-1

841
842 Fanlo, I., Touray, J. C., Subias, I., and Fernandez-Nieto, C. 1998. Geochemical patterns of a
843 sheared fluorite vein, Parzan, Spanish Central Pyrenees. *Mineralium Deposita*, **33**, 620-632.

844
845 Fillon, C., Mouthereau, F., Calassou, S., Pik, R., Bellahsen, N., Gautheron, C., Stockli, D.
846 Brichau, S., Daril, N., Mouchéné, M. and Van der Beek, P. 2021. Post-orogenic exhumation in

847 the western Pyrenees: evidence for extension driven by pre-orogenic inheritance. *Journal*
848 *Geological Society London*, **178**, doi.org/10.1144/jgs2020-079.

849

850 Fontes, J. C. and Matray, J. M. 1993. Geochemistry and origin of formation brines from the
851 Paris Basin, France: 1. Brines associated with Triassic salts. *Chemical Geology*, **109**, 149-175
852

853 Ford, M., and Verges J. 2020. Evolution of a salt-rich transtensional rifted margin, Eastern
854 North Pyrenees, France. *Journal of the Geological Society of London*,
855 doi.org/10.1144/jgs2019-157

856

857 Gleeson, S.A., Yardley, B.W.D, Munz, I.A., and Boyce, A.J. 2003. Infiltration of basinal fluids
858 into high-grade basement, South Norway: sources and behaviour of waters and brines.
859 *Geofluids*, **3**, 33– 48.

860

861 Golberg, J. M., and Maluski H. 1988, Données nouvelles et mise au point sur l'âge du
862 métamorphisme pyrénéen. *Compte-Rendus Académie Sciences*, **306**, 429-435.

863

864 Grandia, E., Cardellach, E., Canals, A. and Banks, D.A. 2003a. Geochemistry of the fluids
865 related to epigenetic carbonate-hosted Zn-Pb deposits in the Maestrat Basin, Eastern Spain:
866 fluid inclusion and isotope (Cl, C, O, S, Sr) evidence. *Economic Geology*, **98**, 933-954.
867

868 Grandia, F., Canals, A., Cardellach, E., Banks, D.A and Perona, J. 2003b. Origin of ore-forming
869 brines in sediment-hosted Zn-Pb deposits of the Basque-Cantabrian Basin, Northern Spain.
870 *Economic Geology*, **98**, 1397-1411.

871

872 Hovland, M., Rueslåtten, H. and Johnsen, H.K. 2018, Large salt accumulations as a
873 consequence of hydrothermal processes associated with 'Wilson cycles': A review, Part 2:
874 Application of a new salt-forming model on selected cases. *Marine Petroleum Geology*, **92**,
875 128-148.

876

877 Incerpi, N., Manatschal, G., Martire, L., Bernasconi, S.M., Gerdes, A. and Bertok, C. 2020.
878 Characteristics and timing of hydrothermal fluid circulation in the fossil Pyrenean

879 hyperextended rift system: new constraints from the Chaînons Béarnais (W Pyrenees).
880 *International Journal of Earth Sciences*, doi.org/10.1007/s00531-020-01852-6.
881
882 Izquierdo-Llavall, E., Menant, A., Aubourg, C., Callot, J.-P., Hoareau, G., Camps, P., Péré, E.
883 and Lahfid, A. (2020) Preorogenic Folds and Syn-Orogenic Basement Tilts in an Inverted
884 Hyperextended Margin: The Northern Pyrenees Case Study. *Tectonics*, **39**, e2019TC005719.
885
886 Jackson, M.P.A. and Talbot, C.J. 1986. External shapes, strain rates, and dynamics of salt
887 structures. *GSA Bulletin*, **97**, 305–323.
888
889 James, V. and Canérot, J. 1999. Diapirisme et structuration post-triasique des Pyrénées
890 occidentales et de l'Aquitaine méridionale (France). *Eclogae Geologica Helvetica*, **92**, 63-72.
891
892 Jammes, S., Manatschal, G. and Lavier, L. 2010. Interaction between prerift salt and
893 detachment faulting in hyperextended rift systems: The example of the Parentis and
894 Mauléon basins (Bay of Biscay and western Pyrenees). *AAPG Bulletin*, **94**, 957–975.
895
896 Jammes, S., Manatschal, G., Lavier, L. and Masini, E. 2009. Tectonosedimentary evolution
897 related to extreme crustal thinning ahead of a propagating ocean: example of the western
898 Pyrenees. *Tectonics*, **28**, TC4012, doi:10.1029/2008TC002406
899
900 Johnson, C.A., Cardellach, E., Tritlla, J. and Hanan, B.B. 1996. Cierco Pb-Zn-Ag vein deposits:
901 Isotopic and fluid inclusion evidence for Formation during the Mesozoic extension in the
902 Pyrenees of Spain. *Economic Geology*, **91**, 497-506.
903
904 Jolivet, M., Labaume, P., Monié, P., Brunel, M., Arnaud, N., and Campani, M. 2007.
905 Thermochronology constraints for the propagation sequence of the South-Pyrenean
906 basement thrust system (France-Spain). *Tectonics*, **26**,
907 <http://dx.doi.org/10.1029/2006TC002080>.
908

909 Labaume, A. and Teixell, A. 2020. Evolution of salt structures of the Pyrenean rift (Chaînons
910 Béarnais, France): Form hyperextension to tectonic inversion. *Tectonophysics*, **785**, 228451
911 doi: 10.1016/j.tecto.2020228451.
912

913 Labaume, P., Meresse, F., Jolivet, M., Teixell, A. and Lahfid, A. 2016. Tectonothermal history
914 of an exhumed thrust-sheet-top basin: An example from the south Pyrenean thrust belt.
915 *Tectonics*, **35**, 1280-1313, <https://doi.org/10.1002/2016TC004192>
916

917 Lacroix, B., Buatier, M., Labaume, P., Trave, A., Dubois, M., Charpentier D., Ventalon, S., and
918 Convert-Gaubier, D. 2011. Microtectonic and geochemical characterisation of thrusting in a
919 foreland basin: Example of the South-Pyrenean orogenic wedge (Spain). *Journal of Structural*
920 *Geology*, **33**, 1359-1377.
921

922 Lagabrielle, Y., Asti, R., Fourcade, S., Corre, B., Poujol, M., Uzel, J., Labaume, P., Clerc, C.,
923 Lafay, R., Picazo, S. and Maury, R. 2019a. Mantle exhumation at magma-poor passive
924 continental margins. Part I. 3D architecture and metasomatic evolution of a fossil exhumed
925 mantle domain (Urdach lherzolite, north-western Pyrenees, France). *Bulletin de la Société*
926 *Géologique de France*, **190**, 8. doi.org/10.1051/bsgf/2019007
927

928 Lagabrielle, Y., Asti, R., Fourcade, S., Corre, B., Uzel, J., Labaume, P., Clerc, C., Lafay, R. and
929 Picazo S. 2019b. Mantle exhumation at magma-poor passive continental margins. Part II.
930 Tectonic and metasomatic evolution of large-displacement detachment faults preserved in a
931 fossil distal margin domain (Sarailé lherzolites, north-western Pyrenees, France). *Bulletin de*
932 *la Société Géologique de France*, **190**,14. doi.org/10.1051/bsgf/2019013
933

934 Lagabrielle, Y., Asti, R., Duretz, T., Clerc, C., Fourcade, S., Teixell, A., Labaume, P., Corre, B.
935 and Saspiturry, N. 2020. A review of cretaceous smooth-slopes extensional basins along the
936 Iberia-Eurasia plate boundary: How pre-rift salt controls the modes of continental rifting and
937 mantle exhumation. *Earth Science Reviews*, **201**, 103071.
938 doi.org/10.1016/j.earscirev.2019.103071
939

940 Leleu, S., Hartley, A., vanOosterhout, C., Kennan, L., Ruckwied, K. and Gerdes, K. 2016.
941 Structural, Stratigraphic and sedimentological characterisation of a wide rift system: The
942 Triassic rift system of the Central Atlantic Domain. *Earth Science Reviews*,
943 doi:10.1016/j.earscirev.2016.03.008
944

945 Levet, S., Toutain, J. P. , Munoz, M., Berger, G., Negrel, P., Jendrzewski, N., Agrinier, P.
946 and Sortino, F. 2002. Geochemistry of the Bagnères-de-Bigorre thermal waters from the
947 North Pyrenean Zone (France). *Geofluids*, <https://doi.org/10.1046/j.1468-8123.2002.00030.x>
948

949 Martz, P., Mercadier, J., Cathelineau, M., Boiron, M.C., Quirt, D., Doney, A., Gerbeaud, O., De
950 Wally, E. and Ledru, P. 2019. Formation of U-rich mineralising fluids through basinal brine
951 migration within basement-hosted shear zones: A large-scale study of the fluid chemistry
952 around the unconformity-related Cigar Lake U deposit (Saskatchewan, Canada). *Chemical*
953 *Geology*, **508**, 116-143.
954

955 Masini, E., Manatschal, G., Tugend, J., Mohn, G. and Flament, J.-M. 2014. The tectono-
956 sedimentary evolution of a hyper-extended rift basin: the example of the Arzacq–Mauléon
957 rift system (Western Pyrenees, SW France). *International Journal of Earth Sciences*, **103**,
958 1569–1596. <https://doi.org/10.1007/s00531-014-1023-8>
959

960 McCaig, A.M., Wayne, D.M., Marshall, J.D., Banks, D.A. and Henderson, I., 1995. Isotopic
961 and fluid inclusion studies of fluid movement along the Gavarnie Thrust, central Pyrenees;
962 reaction fronts in carbonate mylonites. *American Journal of Science*, **295**, 309-343
963

964 McCaig, A.M., Tritlla, J. and Banks, D.A. 2000. Fluid mixing and recycling during Pyrenean
965 thrusting: Evidence from fluid inclusion halogen ratios. *Geochimica Cosmochimica Acta*, **64**,
966 3395-3412.
967

968 Meresse, F. 2010. Dynamique d'un prisme orogénique intracontinental : évolution
969 thermochronologique (traces de fission sur apatite) et tectonique de la Zone Axiale et des
970 piémonts des Pyrénées centro-occidentales. PhD thesis , Montpellier II Univ., 277 p.
971

972 Montigny, R., Azambre, B., Rossy, M., and Thuizat, R. 1986. K-Ar study of cretaceous
973 magmatism and metamorphism in the pyrenees: age and length of rotation of the iberian
974 peninsula. *Tectonophysics*, **129**, 257-213.

975

976 Motte, G., Hoareau, G., Callot, J.P., Révillon, S., Piccoli, F., Calassou, S. and Gaucher, E.C.
977 2021. Rift and salt-related multi-phase dolomitisation: example from the northwestern
978 Pyrenees. *Marine Petroleum Geology*, doi.org/10.1016/j.marpetgeo.2021.104932

979

980 Mouthereau, F., Filleaudeau, P.Y., Vacherat, A., Pik, R., Lacombe, O., Fellin, M.G., Castelltort,
981 S., Christophoul, F. and Masini, E. 2014. Placing limits to shortening evolution in the
982 Pyrenees: role of margin architecture and implications for the Iberia/Europe convergence.
983 *Tectonics*, **33**, 2283-2314. doi:10.1002/2014TC003663.

984

985 Munoz, M., Baron, S., Boucher, A., Beziat, D. and Salvi S. 2015. Mesozoic vein-type Pb–Zn
986 mineralisation in the Pyrenees: Lead isotopic and fluid inclusion evidence from the Les
987 Argentières and Lacore deposits. *Compte-Rendus Geosciences*, **348**, 322-332.

988

989 Nalpas, T. and Brun, J.P. 1993. Salt flow and diapirism related to extension at crustal scale.
990 *Tectonophysics*, **228**, 349-362.

991

992 Nteme Mukonzo, J., Boiron, M.C., Lagabrielle, Y., Cathelineau, M. and Quesnel B. 2021. Fluid-
993 rock interactions along detachment faults during continental rifting and mantle exhumation:
994 the case of the Urdach lherzolite body (North-Pyrenees). *Journal of the Geological Society of*
995 *London*, doi.org/10.1144/jgs2020-116.

996

997 Olivet, J.L. 1996. La cinématique de la plaque ibérique. *Bulletin des Centres de Recherche*
998 *Exploration Production Elf Aquitaine*, **20**, 131–195.

999

1000 Orti, F., Perez-Lopez, A. and Salvany, J.M. 2017. Triassic evaporites of Iberia:
1001 Sedimentological and palaeogeographical implications for the western Neotethys Evolution
1002 during the Middle Triassic–Earliest Jurassic. *Palaeogeography Palaeoclimatology*
1003 *Palaeoecology*, **471**, 157–180.

1004
1005 Parseval, de P. 1992. Étude minéralogique et géochimique du gisement de talc et chlorite
1006 de Trimouns, Ph. D. thesis, Université de Toulouse III.
1007
1008 Poujol, M., Boulvais, P., Kosler, J. 2010. Regional-scale Cretaceous albitisation in the
1009 Pyrenees: evidence from in situ U-Th-Pb dating of monazite, titanite and zircon. *Journal of*
1010 *the Geological Society of London*, **167**, 751-767. doi.org/10.1144/0016-76492009-144
1011
1012 Quesnel, B., Boiron, M.C., Cathelineau, M., Truche, L., Rigaudier, T., Bardoux, G., Agrinier, P.,
1013 de Saint Blanquat, M., Masini, E. and Gaucher, E.C. 2019. Nature and origin of mineralizing
1014 fluids in hyper-extensional systems, the case of Cretaceous Mg-metasomatism in the
1015 Pyrenees. *Geofluids*, doi.org/10.1155/2019/7213050
1016
1017 Rahl, J.M., Haines, S.H. and van der Pluijm, B.A. 2011. Links between orogenic wedge
1018 deformation and erosional exhumation: Evidence from illite age analysis of fault rock and
1019 detrital thermochronology of syn-tectonic conglomerates in the Spanish Pyrenees. *Earth and*
1020 *Planetary Science Letters*, **307**, 180–190.
1021
1022 Renard, S., Pironon, J., Sterpenich, J., Carpentier, C., Lescanne, M. and Gaucher, E. C. 2019.
1023 Diagenesis in Mesozoic carbonate rocks in the North Pyrenees (France) from mineralogy and
1024 fluid inclusion analysis: example of Rousse reservoir and caprock. *Chemical Geology*, **508**, 30-
1025 46. <https://doi.org/10.1016/j.chemgeo.2018.06.017>
1026
1027 Richard, A., Boulvais, P., Mercadier, J., Boiron, M.C., Cathelineau, M., Cuney M. and France -
1028 Lanord, C. 2013. From evaporated seawater to uranium mineralising brines: Isotopic and
1029 trace element study of quartz dolomite veins in the Athabasca system. *Geochimica*
1030 *Cosmochimica Acta*, **113**, 38-59.
1031
1032 Ryan, W. B.F. 2008. Modeling the magnitude and timing of evaporative draw down during
1033 the Messinian salinity crisis. *Stratigraphy*, **5**, 227-243
1034

1035 Salardon, R., Carpentier, C., Bellahsen, N., Pironon, J. and France-Lanord, C. 2016.
1036 Interactions between tectonics and fluid circulations in an inverted hyper-extended basin:
1037 Example of mesozoic carbonate rocks of the western North Pyrenean Zone (Chaînons
1038 Béarnais, France). *Marine Petroleum Geology*, doi: 10.1016/j.marpetgeo.2016.11.018.
1039
1040 Sanchez, V., Vindel, E., Martin-Crespo, M., Corbella, M., Cardellach, E. and Banks D.A. 2009.
1041 Sources and composition of fluids associated with fluorite deposits of Asturias (N Spain).
1042 *Geofluids*, **9**, 338-355.
1043
1044 Sanchez, V., Cardellach, E., Corbella, M., Vindel, E., Martin-Crespo, M. and Boyce, A.J. 2010.
1045 Variability in fluid sources in the fluorite deposits from Asturias (N Spain): Further evidences
1046 from REE, radiogenic (Sr, Sm, Nd) and stable (S, C, O) isotope data. *Ore Geology Reviews*, doi
1047 : 10.1016/j.oregeorev.2009.12001.
1048
1049 Saspiturry, N., Lahfid, A., Baudin, T., Guillou-Frottier, L., Razin, P., Issautier B., Le Bayon, B.,
1050 Serrano, O., Lagabrielle, Y. and Corre, B. 2020. Paleogeothermal gradients across an inverted
1051 hyperextended rift system: Example of the Mauléon fossil rift (Western Pyrenees). *Tectonics*,
1052 doi: 10.17632/47kgv7r9wm.3.
1053
1054 Saura, E., L. Ardèvol i Oró, A. Teixell, and J. Vergés (2016) Rising and falling diapirs, shifting
1055 depocenters, and flap overturning in the Cretaceous Sopeira and Sant Gervàs subbasins
1056 (Ribagorça Basin, southern Pyrenees), *Tectonics*, **35**, 638–662, doi: 10.1002/2015TC004001.
1057
1058 Schärer, U., de Parseval, P., Polvé, M. and de Saint Blanquat, M. 1999. Formation of the
1059 Trimouns talc-chlorite deposit (Pyrenees) from persistent hydrothermal activity between
1060 112 and 97 Ma. *Terra Nova*, **11**, 30–37.
1061
1062 Scribano, V., Carbone, S., Manuella, F.C., Hovland, M., Rueslatten, H. and Johnsen, H.K.
1063 2017. Origin of salt giants in abyssal serpentinite systems. *International Journal of Earth*
1064 *Sciences*, **106**, 2595-2608.
1065

1066 Shao H., Wang, Y., Kolditz O., Nagel T. and Brüning T. 2019. Approaches to multi-scale
1067 analyses of mechanically and thermally-driven migration of fluid inclusions in salt rocks.
1068 *Physics and Chemistry of the Earth*, **113**, 1-13. doi.org/10.1016/j.pce.2019.07.003
1069

1070 Souche, A., Dabrowski, M., Andersen, T.B. 2014. Modeling thermal convection in
1071 supradetachment basins: example from western Norway. *Geofluids*, **14**, 58-74.
1072

1073 Spiers, C.J., Schutjens, P.M.T.M., Brzesowsky, R.H., Peach, C.J., Liezenberg, J.L. and Zwart,
1074 H.J. 1990. Experimental determination of constitutive parameters governing creep of rock
1075 salt by pressure solution. In: Knipe, R.J. and Rutter, E.H. (eds), *Deformation Mechanisms,*
1076 *Rheology and Tectonics. Geological Society Special Publication*, **45**, 215-227.
1077

1078 Steele-MacInnis, M., Bodnar, R.J. and Naden, J. 2011. Numerical model to determine the
1079 composition of H₂O-NaCl-CaCl₂ fluid inclusions based on microthermometric and
1080 microanalytical data. *Geochimica Cosmochimica Acta*, **75**, 21-40.
1081

1082 Stober, I. and Bucher, K. 2004. Fluid sinks within the earth's crust. *Geofluids*, **4**, 143-151
1083

1084 Subias, I. and Fernandez-Nieto C. 1995. Hydrothermal events in the Valle de Tena (Spanish
1085 Western Pyrenees) as evidenced by fluid inclusions and trace-element distribution from
1086 fluorite deposits. *Chemical Geology*, **124**, 267-282.
1087

1088 Subias, I., Fanlo, I., and Billström, K. 2015. Ore-forming timing of polymetallic-fluorite low
1089 temperature veins from Central Pyrenees: A Pb, Nd and Sr isotope perspective. *Ore Geology*
1090 *Reviews*, **70**, 241-251.
1091

1092 Teixell, A., Labaume, P., Ayarza, P., Espurt, N., de Saint Blanquat, M. and Lagabrielle, Y. 2018.
1093 The present-day and past crustal structure of the Pyrenean-Cantabrian belt: a review and
1094 new interpretations from recent concepts and data. *Tectonophysics*, **724-725**, 146-170. DOI:
1095 10.1016/j.tecto.2018.01.009.
1096

1097 Teixell, A. 1996. The Anso´ transect of the southern Pyrenees: basement and cover thrust
1098 geometries. *Journal of the Geological Society of London*, **153**, 301–310.
1099

1100 Teixell, A., Labaume, P. and Lagabrielle, Y. 2016. The crustal evolution of the west-central
1101 Pyrenees revisited: inferences from a new kinematic scenario. *Compte-Rendus Geosciences*,
1102 **348**, 257- 267. doi: 10.1016/j.crte.2015.10.010.
1103

1104 Trincal, V., Lanari, P., Buatier, M., Lacroix, B., Charpentier, D., Labaume, P. and Munoz, M.
1105 2015. Temperature micro-mapping in oscillatory-zoned chlorite: Application to study of a
1106 green-schist facies fault zone in the Pyrenean Axial Zone (Spain). *American Mineralogist*,
1107 **100**, 2468-2483.
1108

1109 Trincal, V., Buatier, M., Charpentier, D., Lacroix, B., Lanari, P., Labaume, P., Lahfid, A., and
1110 Vennemann, T. 2017. Fluid–rock interactions related to metamorphic reducing fluid flow in
1111 meta- sediments: example of the Pic- de- Port- Vieux thrust (Pyrenees, Spain).
1112 *Contributions to Mineralogy and Petrology*, **172**, 78, DOI 10.1007/s00410-017-1394-5.
1113

1114 Tugend, J., Manatschal, G., Kuszniir, N.J., Masini, E., Mohn, G., and Thion, I. 2014. Formation
1115 and deformation of hyperextended rift systems: Insights from rift domain mapping in the
1116 Bay of Biscay-Pyrenees. *Tectonics*, **33**, 1239–1276. <https://doi.org/10.1002/2014TC003529>
1117

1118 Turner, P. and Sherif, H.,2007. A giant Late Triassic – Early Jurassic evaporitic basin on
1119 Saharan platform, North Africa. In *Evaporites through space and time*, *Geological Society of*
1120 *London, Special Publications*, **285**, 87-105.
1121

1122 Urai, J.L., Spiers, C.J., Zwart., H.J. and Lister, G.S. 1986. Weakening of rock salt by water
1123 during long-term creep. *Nature*, **324**, 554-557.
1124

1125 Urai, J.L., Schleder, Z., Spiers, C.J. and Kukla, P.A. 2008. Flow and transport properties of
1126 saltrocks. In: Littke, R., Bayer, U., Gajewski, D., Nelskamp, S., editors. *Dynamics of complex*
1127 *intracontinental basins: The Central European Basin System*. Berlin, Springer, 277–90.
1128

1129 Vacherat, A., Mouthereau, F., Pik, R., Bernet, M., Gautheron, C., Masini, E., Le Pourhiet, L.,
1130 Tibaric, B., and Lahfid, A. 2014. Thermal imprint of rift-related processes in orogens as
1131 recorded in the Pyrenees. *Earth and Planetary Science Letters*, **408**, 296–306.
1132

1133 Vacherat, A., Mouthereau, F., Pik, R., Bellahsen N., Gautheron, C., Bernet, M., Daudet M.,
1134 Balansa J., Tibari B., Pina Jamme R., Radal J. 2016. Rift-to-collision transition recorded by
1135 tectonothermal evolution of the northern Pyrenees. *Tectonics*, **35**, 907-933,
1136 <https://doi.org/10.1002/2015TC004016>
1137

1138 Vendeville, B.C., Ge, H. and Jackson, P.A. (1995). Scale models of salt tectonics during
1139 basement-involved extension. *Petroleum Geosciences*, **1**, 179-183.
1140

1141 Vissers, R.L.M., Ganerod, M., Pennock, G.N. and Van Hinsbergen, D.J.J. 2020. Eocene
1142 seismogenic reactivation of a Jurassic ductile shear zone at Cap de Creus, Pyrenees, NE
1143 Spain. *Journal of Structural Geology*, **134**, 103994.
1144

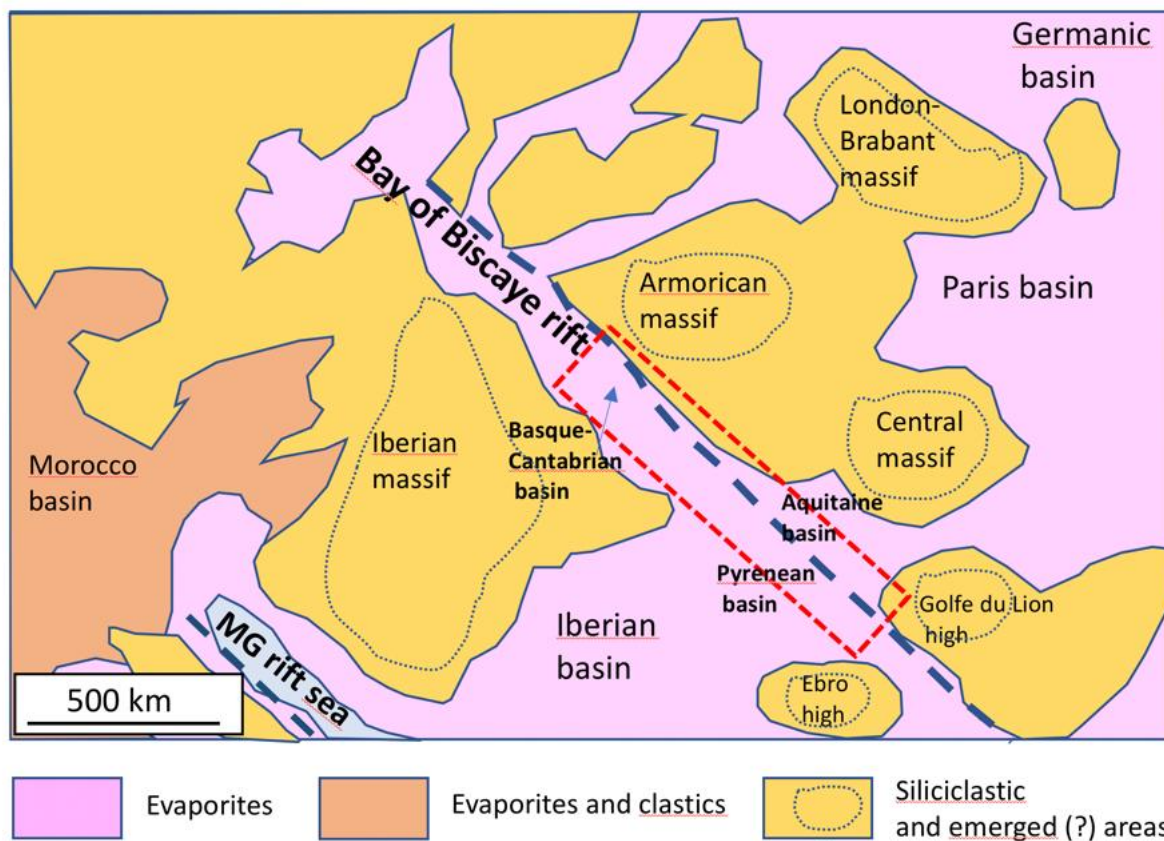
1145 Walter, B.F., Burisch, M. and Markl, G. 2016. Long-term chemical evolution and modification
1146 of continental basement brines - a field study from the Schwarzwald, SW Germany. *Geofluid*,
1147 **16**, 604–623. <http://dx.doi.org/10.1111/gfl.12167>.
1148

1149 Van Keken, P. E., Spiers, C.J., van den Berg, A.P. and Muzyert, E.J. 1993. The effective
1150 viscosity of rock salt: implementation of steady-state creep laws in numerical models of salt
1151 diapirism. *Tectonophysics*, **225**, 457-476, [https://doi.org/10.1016/0040-1951\(93\)90310-G](https://doi.org/10.1016/0040-1951(93)90310-G)
1152

1153 Wayne, D.M. and McCaig, A. M. 1998. Dating fluid flow in shear zones: Rb-Sr and U-Pb
1154 studies of syntectonic veins in the Néouvielle Massif, Pyrenees. *Geological Society of London*
1155 *Special Publications*, **144**, 129-135. DOI: 10.1144/GSL.SP.1998.144.01.09
1156
1157

1158 **Figure captions**

1159



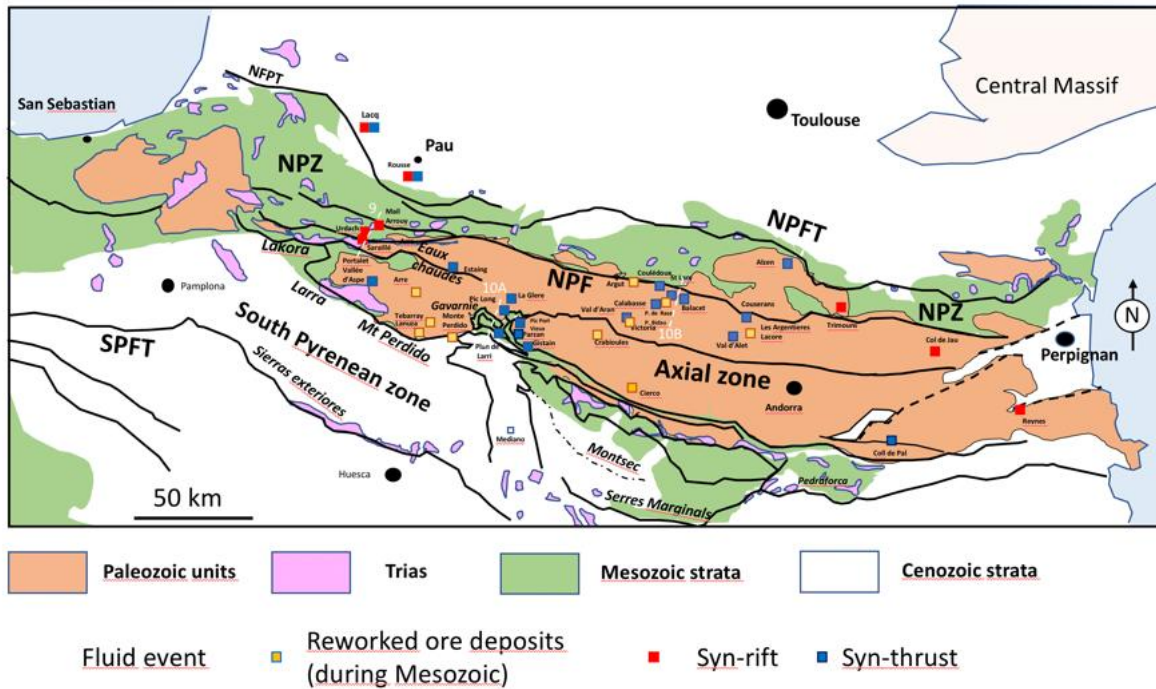
1160

1161

1162

1163 Fig. 1: Distribution of predominant Triassic evaporites (in pink) in southern Europe with an
1164 indication of the Pyrenean area from a palaeogeographic map for late Triassic slightly
1165 modified from Orti et al. (2017); MG: Maghrebian-Gibraltar.

1166



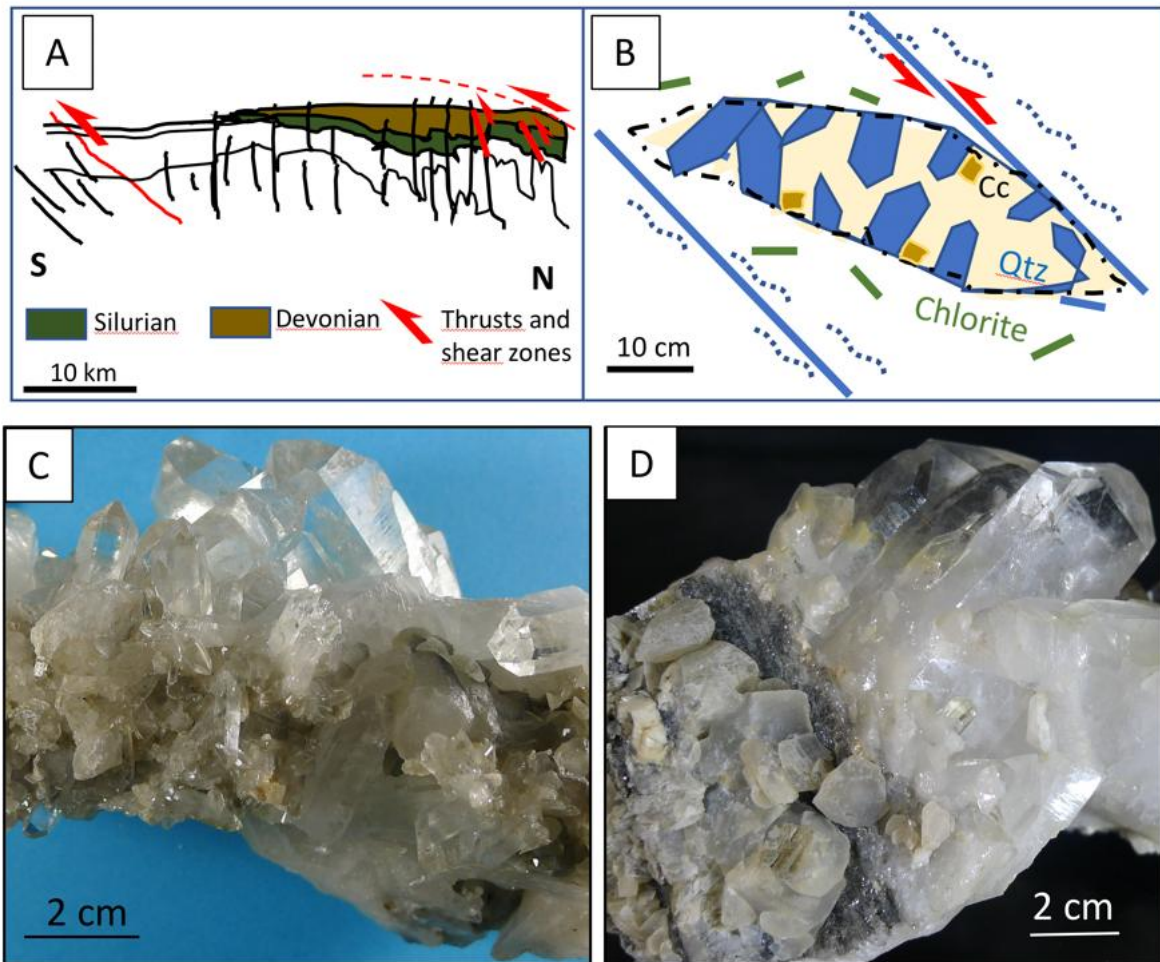
1167

1168

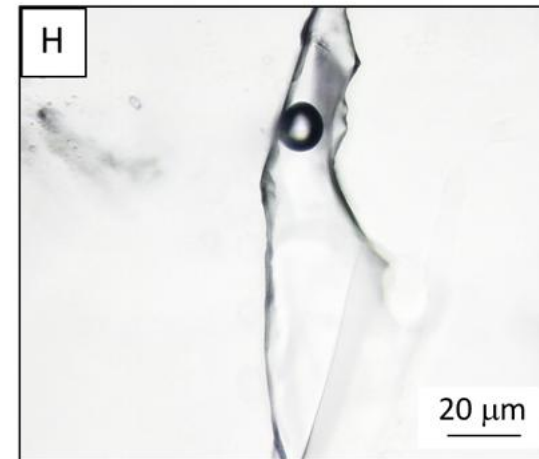
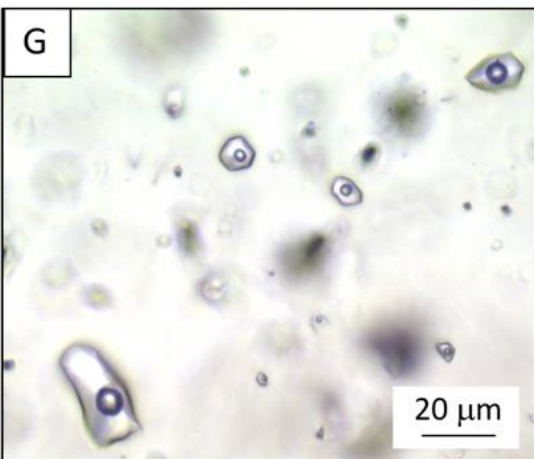
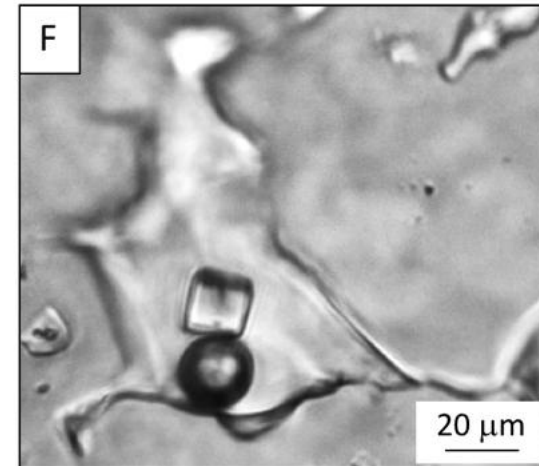
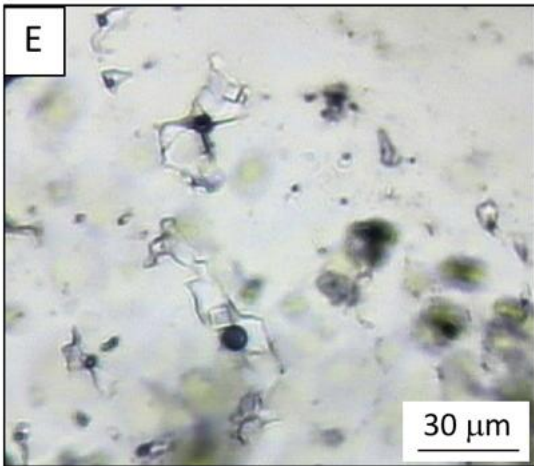
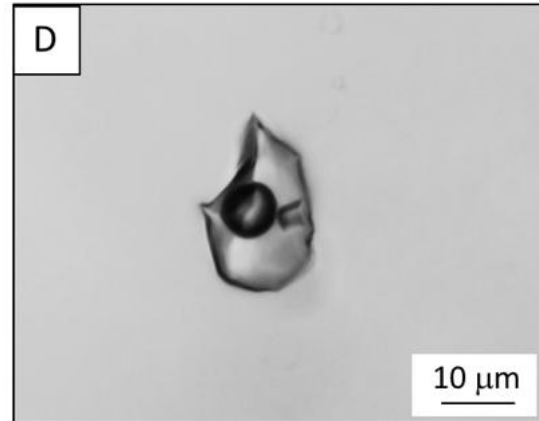
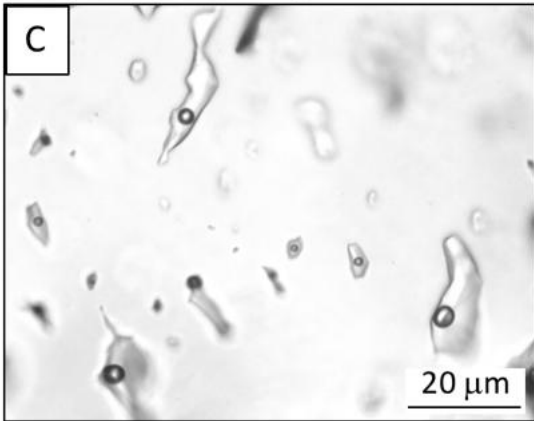
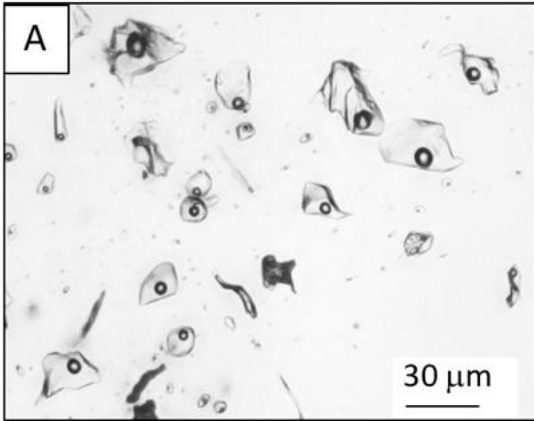
1169 Fig. 2: Distribution of the studied localities in the Pyrenees chain reported on a geological
 1170 map modified from Ford and Verges (2020). Red points correspond to localities for which
 1171 new data have been acquired during the present work. White circles with a red dot
 1172 correspond to localities described in the literature. NPF: North Pyrenean Fault, NPFT: North
 1173 Pyrenean Frontal Thrust, SPFT: South Pyrenean Frontal Thrust. The approximative locations
 1174 of the cross-section shown in Fig. 9, 10A and 10B are indicated as white dashed lines.



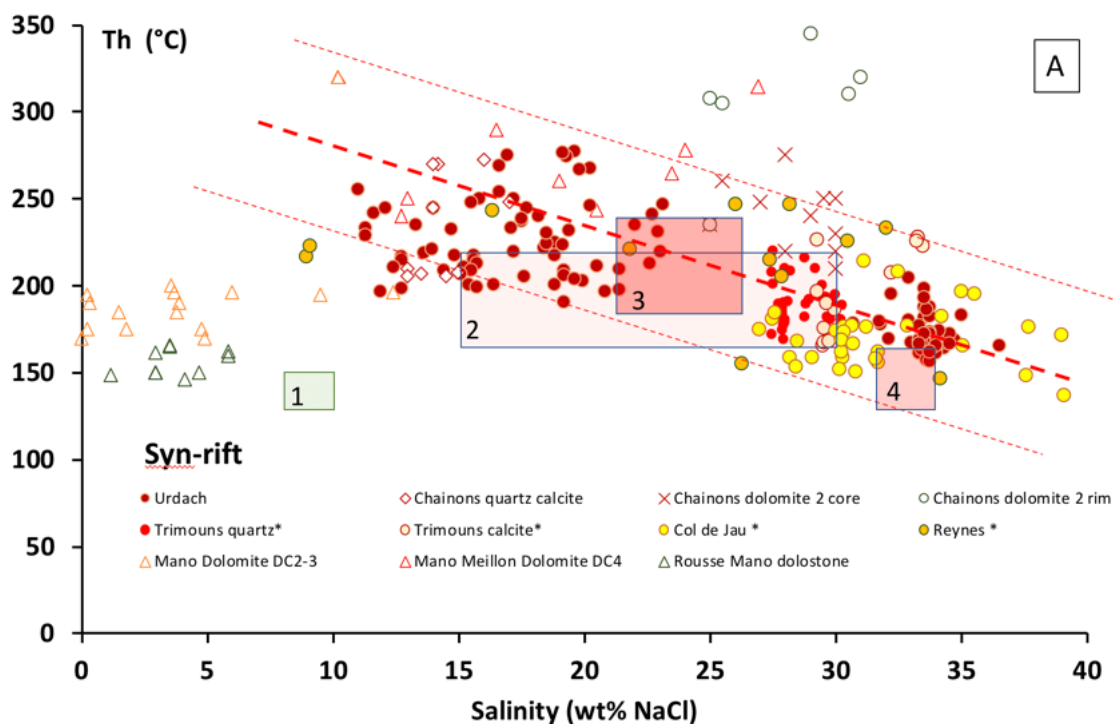
1175
 1176 Fig. 3: Macroscopic features of studied samples: A: silicified breccia from basement/ Trias
 1177 interface (Urdach, Chaînons Bearnais). B: dolomite cemented breccia in Mano formation
 1178 (Mail Arrouy, Chaînons Bearnais); C: prismatic quartz embedded in calcite, from Mg-
 1179 metasomatic zone (Col de Jau, eastern Axial zone); D: euhedral bi-terminated quartz prism
 1180 on dolomite and talc from Mg-metasomatic zone (Trimouns, Saint Barthelemy massif).



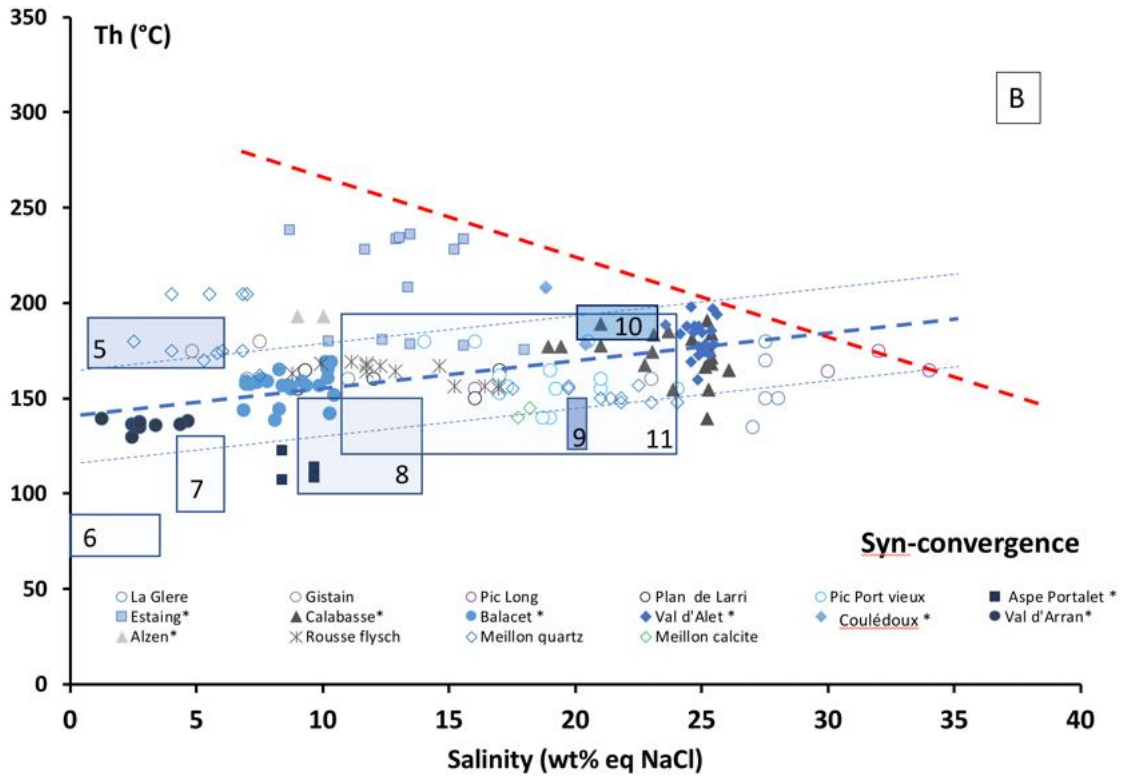
1181
 1182 Fig. 4: A: Simplified cross-section of Ariège/ Haute Garonne region close to the North
 1183 Pyrenean Fault (NPF, see Fig. 2). B; Schematic cross-section of a tension gash developed in
 1184 relation with reactivated shear planes. Qtz: quartz, CC: calcite; C: Macroscopic features of
 1185 euhedral quartz from Val d'Alet (Ariège, Axial zone); D: euhedral quartz from Balacet (Ariège,
 1186 Axial zone).



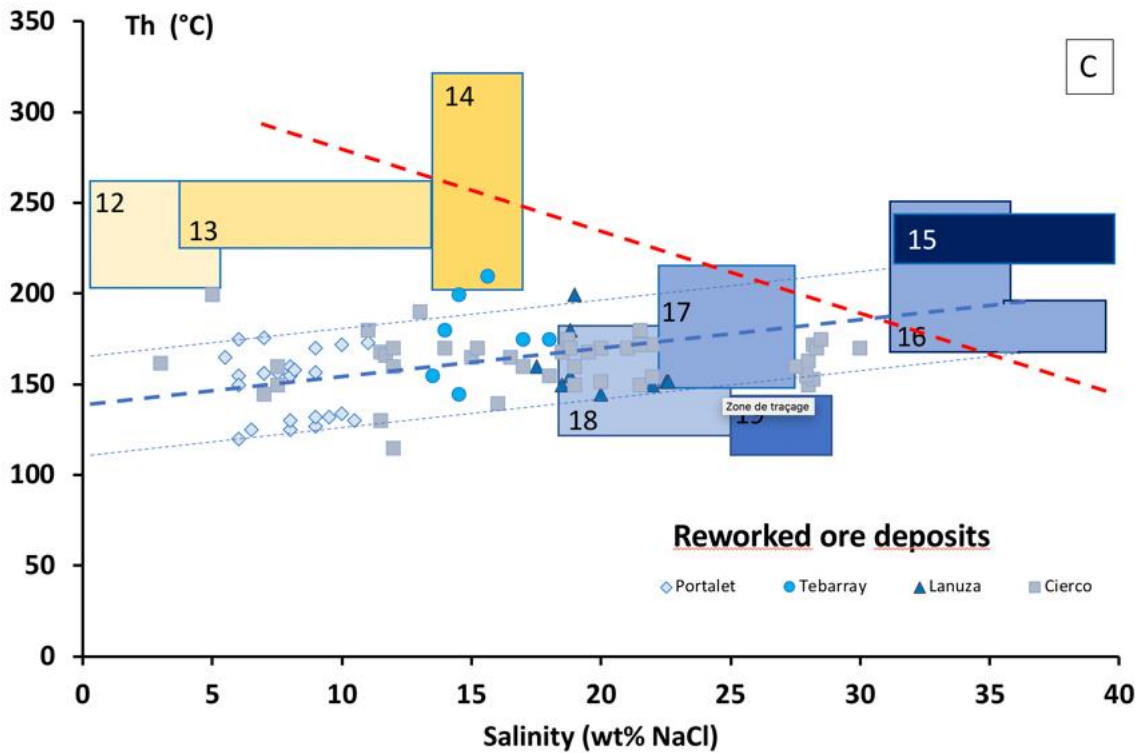
1188 Fig. 5: Fluid inclusion types: A: two-phase fluid inclusions (Lw Fis) from Val d'Alet quartz; B:
 1189 three-phase fluid inclusion with a halite cube (Lwh Fi) from Val d'Alet quartz; C: two-phase
 1190 fluid inclusions (Lw Fis) from La Calabasse; D: three-phase fluid inclusions (Lwh Fi) from La
 1191 Calabasse; E: three-phase fluid inclusions (Lwh Fis) from Col de Jau; F: three-phase fluid
 1192 inclusion with a halite cube from Etche, Urdach massif (Lwh Fi); G: two-phase fluid inclusions
 1193 from St Lary (Lw Fis); H: two-phase fluid inclusion (Lw) from Val d'Aran.



1194



1195



1196

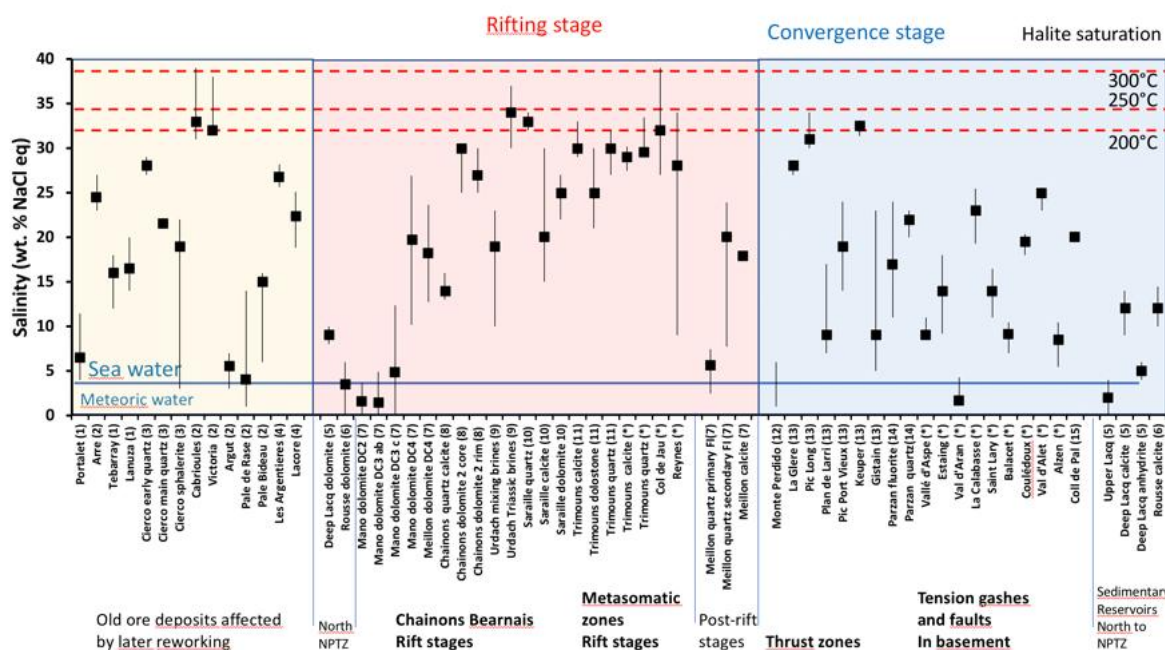
1197

1198 Fig. 6: Synthetic Tm-Th plot of fluid inclusion data for Mesozoic and syn-rift (A), syn-thrust

1199 paleofluids (B) events, and reworked ore deposits (C). Full coloured symbols correspond to

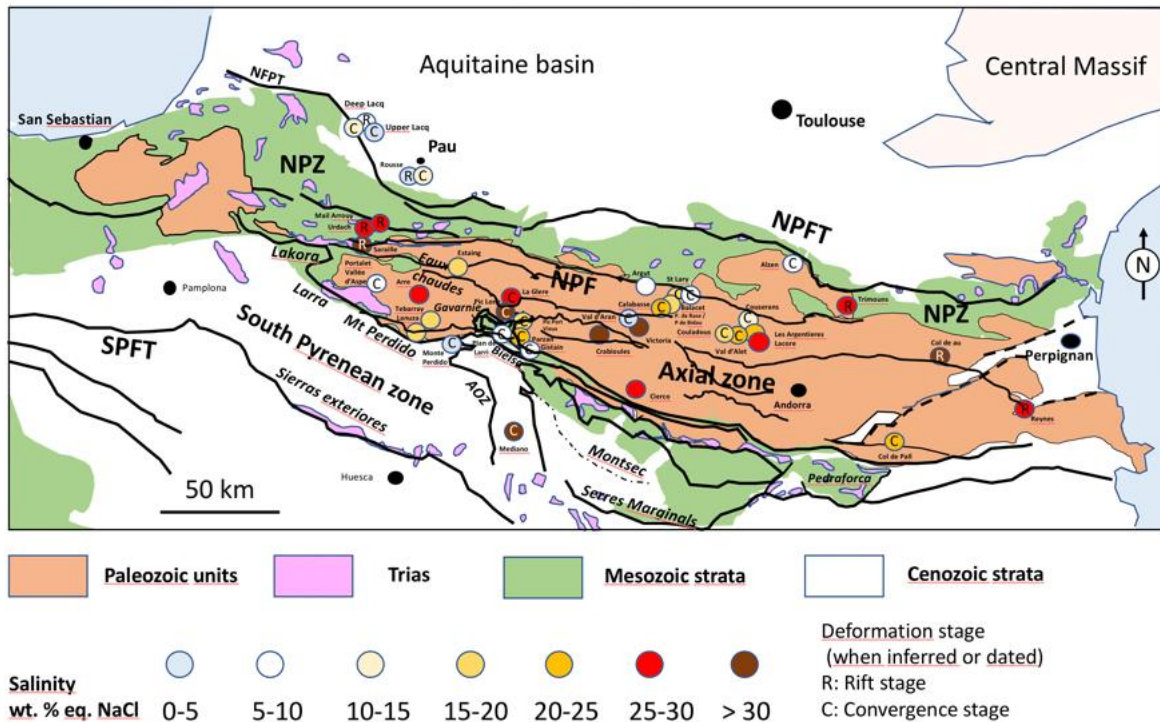
1200 new data (noted with *) and other symbols to literature data. When salinity-Th pairs are
 1201 lacking, domains have been drawn using ranges and modes given by the authors. Dashed
 1202 lines indicate main mixing trends, red: syn-rift stage, blue: syn-convergence stage.

1203 Literature data: 1 – Deep Lacq (saddle dolomite, Bahnan, 2019), 2 - Saraille calcite, 3 -
 1204 Saraille dolomite, 4 - Saraille quartz, Corre et al. , (2018) ; 5-Monte Perdido, Lacroix et
 1205 al. (2011); 6 – Upper Lacq, dolomite, 7 - Deep Lacq, Anhydrite, 8 - Deep Lacq calcite, Bahnan
 1206 (2019) ; 9 - Coll de Pal, Canals et al. (1999) ; 10- Parzan quartz, 11 – Parzan fluorite, Fanlo et
 1207 al. (1998); 12-Pale de Rase, 13- Argut, 14- Pale de Bidau, 15- Victoria 16- Crabioules, 17-
 1208 Arre, Cugerone, (2019); 18- Lacore, 19- Les Argentières, Munoz et al. (2015); Other data
 1209 points concern the following localities: Rouse (Renard et al., 2019), Gavarnie thrust (Gistain,
 1210 Pic de Larri, Pic Port Vieux, Pic Long and La Glere, Mc Caig et al., 2000), Portalet, Tebarray
 1211 and Lanuza (Subias and Fernandez Nieto, 1995), Cierco (Johnson et al., 1996). Urdach
 1212 (Nteme Mukonzo et al., 2021), Chainons Bearnais (Chainons., calcite quartz and dolomite,
 1213 Salardon et al., 2016).

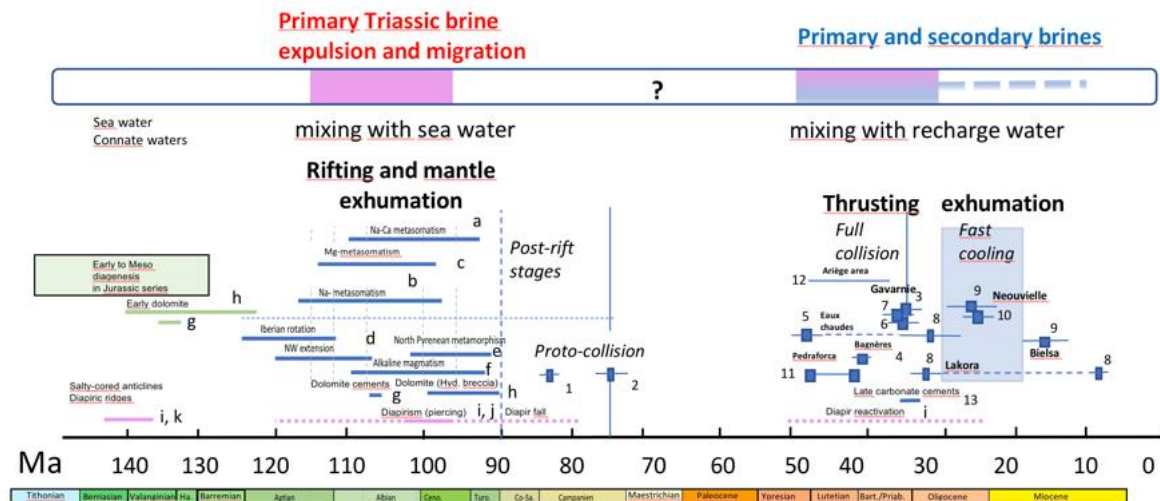


1214 Fig 7: Salinity ranges for all localities, with the indication of halite saturation values and
 1215 seawater salinity. Data are presented in three regions: reworked ore deposits during post-
 1216 Triassic, syn-rift fluid stages, and late fluid circulations attributed to thrusts. SW: seawater.
 1217 References for literature data : 1: Subias and Fernandez Nieto (1995); 2: Cugerone (2019); 3:
 1218 Johnson et al. (1996) ; 4: Munoz et al. (2015) ; 5: Bahnan (2019); 6 : Renard et al. (2019); 7 :
 1219 Motte et al. (2021) ; 8 : Salardon et al. (2016); 9 : Nteme Mukonzo et al. (2021); 10 : Corre
 1220

1221 et al. (2018); 11: Quesnel et al. (2019) ; 12: Lacroix et al. (2011); 13: McCaig et al. (2000) ;
 1222 14: Fanlo et al. (1998); 15: Canals et al. (1999).

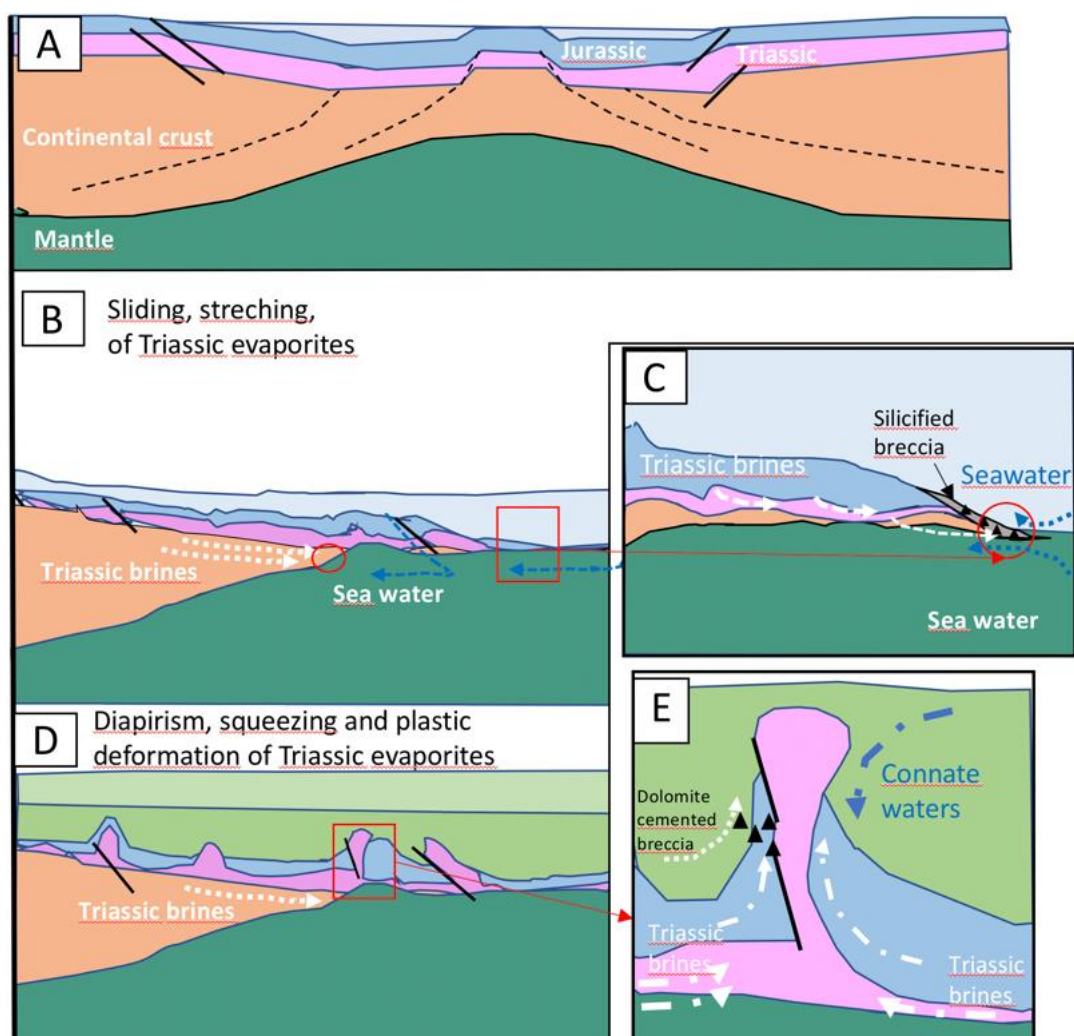


1223
 1224 Fig. 8: Map of distribution of salinities of palaeofluids found in newly formed minerals in
 1225 fractures at the scale of Pyrenees, with an indication of outcropping Upper Trias, major
 1226 faults and thrust (NFPT North Pyrenean Frontal Thrust, NPF: North Pyrenean Fault). C in
 1227 circles for localities attributed to syn-convergence events.



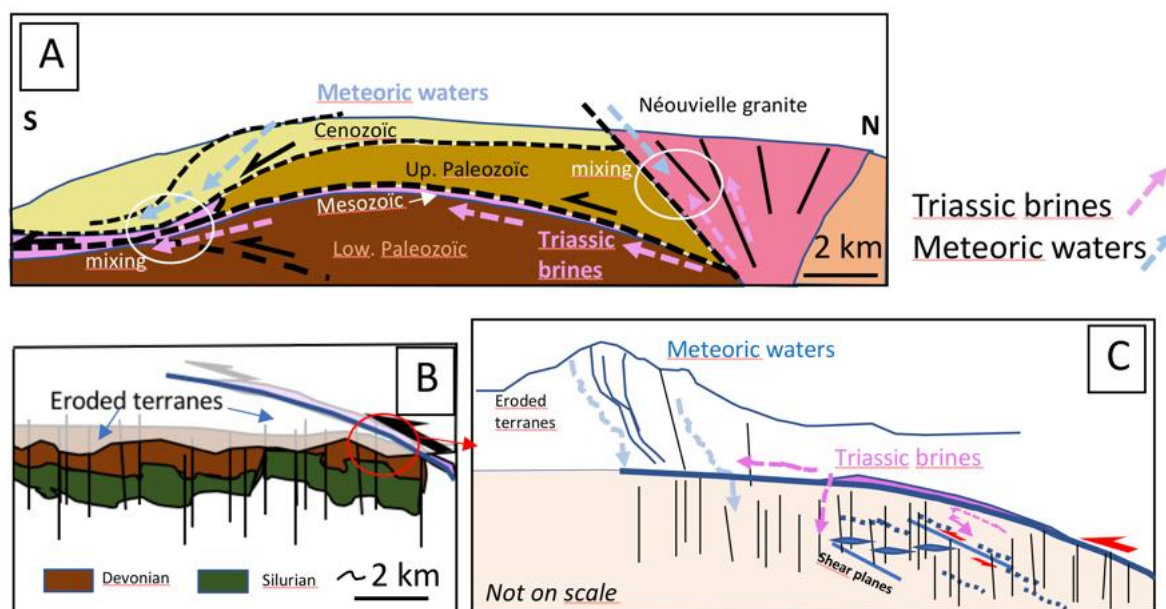
1228
 1229 Fig. 9: Main periods of brine migration in the Pyrenees during Mesozoic and Cenozoic. Ages
 1230 are issued from literature: **Rifting stage** - a: Fallourd et al. (2014); b: Schärer et al. (1999),
 1231 Boutin et al. (2016); c: Poujol et al. (2010), Boutin et al. (2016); d: Jammes et al., (2010); e:

1232 Olivet (1996); f: Goldberg and Maluski (1988); g: Montigny et al. (1986); g : Motte et al.
 1233 (2021), h : Incerpi et al. (2020); i : Canérot et al. (2005) ; j : Saura et al. (2015) ; k : James et
 1234 Canérot (1999) - **Thrusting and exhumation stages** - 1: Vacherat et al. (2014); 2:
 1235 Mouthereau et al. (2014); 3: Teixell (1996); 4: Meresse (2016); 5: Wayne and McCaig (1998);
 1236 6: Rahl et al. (2011); 7: Jolivet et al. (2007) for Gavarnie; 8: Bosch et al. (2016); 9: Jolivet et al.
 1237 (2007) for Neouvielle area, 10 : Labaume et al. (2016), 11 : Cruset et al., 2020, 12 : Vacherat
 1238 et al., 2016; 13 : Renard et al., 2019.



1239
 1240 Fig. 10: Conceptual model of fluid circulation. A: pre-extension stage (A) shown to emphasise
 1241 the continuous cover of a thick evaporite bearing Triassic series before the deformation; B
 1242 and C: the mid-Cretaceous extensional stage followed by and the diapir piercing stage
 1243 (simplified cross-sections modified from Teixell et al. (2016) and Duretz et al. (2020)). C:
 1244 Triassic brines migrate at the boundary between the Paleozoic basement and sedimentary

1245 cover and mix in highly deformed zones corresponding to the mantle sedimentary cover
 1246 interface. They mix with seawater heated at depth and have interacted with mantle rocks
 1247 (serpentinisation process). The mixing is anisothermal as the seawater trajectories above the
 1248 thermal anomalies linked to the mantle uplift are far more heated than brines (anisothermal
 1249 mixing from Fig. 6A). A temperature drop during mixing yield quartz cementation of
 1250 hydraulic breccia (as shown in the Urdach example by Nteme Mukonzo et al., 2021). D and E:
 1251 fluids are issued from further squeezing of evaporites during diapirism stimulated by
 1252 deformation and faulting (Canérot et al., 2004). Triassic brines may mix with several kinds of
 1253 fluids (seawater, connate waters), as proposed by Motte et al. (2021) on the example of Mail
 1254 Arrouy area.



1255
 1256 Fig. 11: Model of fluid circulation during thrusting. A- example of the Gavarnie thrust based
 1257 on a cross-section slightly modified from Jolivet et al. (2007) and Trincal et al. (2015). B
 1258 example, in the Ariège/ Haute Garonne area, where the Paleozoic basement characterised
 1259 by a subvertical foliation, particularly Devonian marbles and quartzites are outcropping due
 1260 to denudation of the overlying thrust zones. C: series of brittle structures developed close to
 1261 shearing planes in the area shown in B.

1262
 1263

1264 **Table Caption**

1265

1266

Locality	Host-rock lithology	Geodynamic event	Mineral hosting Fis	Salinity (wt.% NaCl eq.)		Homogenization temperature(°C)		Gas (as traces)
				range	mode	range	mode	
Trimouns	Dolomite and Chlorite-micaschists	Syn - rift	Quartz (talc)	27.5-30.2	29	168 - 220	190-220	N ₂ -CO ₂ -CH ₄
	Dolomite and Chlorite-micaschists		Calcite	29.3 to 33.5	29.5	166 - 226	190-220	N ₂ -CO ₂ -CH ₄
Col de Jau	Querigut granite-Ordovician Paleozoic schists	Syn - rift	Quartz (talc)	30-33	30	150 - 196	160	N ₂ -CO ₂
Reynès	Paleozoic series undifferentiated	Syn - rift	Quartz (Chlorite-talc)	27-35	29	155 - 247		CO ₂ -N ₂ -CH ₄
Vallée d'Aspe (La Cristallère)	Permian pelites/ Visean marbles	Thrust	Quartz (albite-chlorite)	6.5-10.5	7.9	nd		
Vallée d'Aspe (Portalet)	Permian pelites or Devonian	Thrust	Quartz	8.4-11	9.2	108 - 114	110	
Estaing	Hercynian granite / Devonian marbles	Thrust	Quartz	9.2-17.9	14	176 - 236	230	
Val d'Aran	Devonian series	Thrust	Quartz	1.2-4.3	1.7	129 - 139	135	N ₂ - (CH ₄ , CO ₂)
La Calabasse	Devonian- Dolomitic marbles	Thrust	Quartz-ankerite	19.3-26	23	140 - 190	175	CO ₂ -(N ₂ , CH ₄)
St Lary	Devonian- Dolomitic marbles	Thrust	Quartz	11-16.5	14	209 - 235	225	CO ₂
Balacet	Devonian dolomite	Thrust	Quartz	6.9-10.5	9.2	138 - 169	135	
Couserans	Devonian dolomite	Thrust	Quartz	11.0-11.4	11.2	140 - 220		
Couledoux (Col de l'Artigasou)	Mid-Devonian dolomites	Thrust	Quartz	18-20.3	19.5	168 - 208	180	
Val d'Alet	Devonian dolomite	Thrust	Quartz	23-25	25	160 - 198	185	N ₂ - (CH ₄ , CO ₂)
Mine Alzen	Devonian limestones	Thrust	Calcite	5.7-10.5	8.5	185 - 195	190	

1267

1268 Table 1: Overview of geological occurrences studied in this paper and related fluid inclusion
1269 data. The list includes occurrences of quartz filled tension gashes interpreted as syn-
1270 convergence, as well as syn-rift metasomatic areas.

Locality	Host-rock lithology	Geodynamic event	Mineralisation	Salinity	Salinity mode	Homogenisation temperature	Cl/Br	Traces of gas	References
				wt. % NaCl eq.	wt. % NaCl eq.	°C			
Deep Lacq	Jurassic	Syn-rift	Saddle dolomite	8 - 10	9	130-150		CH ₄ - H ₂ S	Bahnan, 2019
Roussé	Mano dolostone	Syn - rift	Dolomite-calcite	0 - 6	3.5	145-165		CH ₄ -CO ₂ ,hydrocarbons	Renard et al., 2019
Chalons Béarnais	Tithonian Mano formation	Syn-rift	Dolomite DC2	0 - 3.6	1.6	170 -200			Motte et al., 2021
			Dolomite DC3 ab	0 - 5	1.5	150 -190			
			Dolomite DC3c	0 - 12	5	170 -200			
			Dolomite DC4	10 - 27	20	200 -320			
	Oxé-Calloviaian (Meillon)	Syn-rift	Dolomite DC4	13 -24	18	240 - 260			Motte et al., 2021
Chalons Béarnais	Veins in Cretaceous formations	Syn - rift	Quartz and calcite	13 - 16	14	140-220		CO ₂ -N ₂	Salandon et al., 2016
			Dolomite 2 core	25 - 30	30	200-260		CO ₂ -N ₂ -H ₂ S	
			Dolomite 2 rim	25 - 30	27	300-350		CO ₂ -N ₂	
Urdach	Breccia Albian Cenomanian	Syn - rift	Breccia cements	10 - 23	19	200-280	2000-2300	CO ₂ -CH ₄ -N ₂	Nieme Mukonzo et al., 2021
				30 - 37	34	155-200		CO ₂ -CH ₄ -N ₂	
Saraille	Veins in Neocomian Aptian	Syn - rift	Quartz	32 - 34	33	130-160		N ₂ - CH ₄ - H ₂ S	Core et al., 2018
			Calcite	15-30	20	160-220			
Trimouns	Siluro-Devonian micaschists and dolostones	Syn - rift	Dolomite	22-27	25	180-240			
			Calcite	29-33	30	130-230	300-400	CO ₂ -CH ₄ -N ₂	Quesnel et al., 2019
			Dolostone-talc	21-30	25	130-230	270-360	CO ₂ -CH ₄ -N ₂	
			Quartz	27-32	29	130-230	430-610	CO ₂ -CH ₄ -N ₂	
Chalons Béarnais	Meillon formation	Post - rift	Quartz (primary FI)	2.5 - 7.5	5.5	135 - 205			Motte et al., 2021
	Meillon formation	Post - rift	Quartz (secondary FI)	8 - 24	20	140 - 160			
	Meillon formation	Exhumation	Calcite	18	18	140 -160			
Monte Perdidó	Lower Ypresian Millans marls	Convergence stage-Thrust	Quartz and calcite	1 - 6		165-190			Lacroix et al., 2011
Gavarrie thrust									Banks et al.,1991; Mc Caig et al., 1995,2000
Gistain	Triassic red beds (close unconformity with Devonian phyllites)	Convergence stage-Thrust	Quartz barite	5 - 23	9	160-175	440 -3040		McCaig et al., 2000
Plan de Larri	Triassic red beds	Convergence stage-Thrust	Quartz	7 - 17	9	150-180	130-1000		McCaig et al., 2000
Pic Long	Neovielle granite	Convergence stage-Thrust	Quartz	30-34	31	135-175	90-220		McCaig et al., 2000
La Glere	Neovielle granite	Convergence stage-Thrust	Quartz	27-28	28	150-230	90-250		McCaig et al., 2000
Pic Port Vieux	Cambro-Ordovician petites	Convergence stage-Thrust	Quartz	14-24	19	140-180	270-460		McCaig et al., 2000
Keuper	Mediano dolomites	Convergence stage-Thrust	Dolomite	31.4-32.8	32.5	115	460-480		McCaig et al., 2000
Parzan	Vein (boundary granite and Triassic)	Multistage -Mesozoic reworking	Fluorite, Zn	11 - 24	17	120-195			Fanlo et al., 1998
			Quartz	20 - 23	22	180-200			
Coll de Pal	Devonian and Cambrian carbonates	Convergence stage-Thrust ?	Barite and minor Cu sulphide	20	20	125-150			Canals et al., 1999
Upper Lacq	Albian Aptian	Convergence stage-fault	Dolomite, calcite	0 - 4	2	70-90			Bahnan et al., 2020
Deep Lacq	Triassic and Jurassic series	Post-rift (early convergence)	Calcite	9 - 14	12	100-150		CH ₄ - H ₂ S	Bahnan, 2019
			Anhydrite	4 - 6	5	90-130			
Roussé	Campanian flysch	Convergence stage-fault	Calcite	10 - 14.5	12	155-170		CH ₄ -CO ₂	Renard et al., 2019
Portalet	Lower carboniferous limestones	Reworked ore deposits	Fluorite	4 - 11.5	6.5	110-200			Subias and Fernandez Nieto, 1995
Tebar ray	Upper devonian marbles	Reworked ore deposits	Zn-F (Pb) Fluorite	12 -18	16	150-210			Subias and Fernandez Nieto, 1995
Lanuzza	Lower devonian limestones	Reworked ore deposits	Fluorite ± calcite	14-20	16.5	140-220			Subias and Fernandez Nieto, 1995
Cierco	Devonian metasediment, Trias	Reworked ore deposits	Pb-Zn-Ag						
			Early quartz	28	28	152-173	260		
			Main quartz	22	21.5	150-190			
			Sphalerite	5 - 22	19	112-198	170-300		Johnson et al, 1996
Arre	Devonian calcschists	Reworked ore deposits	Quartz (Pb-Zn)	23-27	24.5	160-210			Cugeronne, 2019
Crabioules	Late ordovician Metamorphic schists	Reworked ore deposits	Quartz (Pb-Zn)	31-39	33	220-250			Cugeronne, 2019
Victoria	Late ordovician Metamorphic schists	Reworked ore deposits	Quartz (Pb-Zn)	32-38	32	220-235			Cugeronne, 2019
Argut	Late Ordovician Calcshists	Reworked ore deposits	Quartz (Pb-Zn)	3-7	5.5	230-280			Cugeronne, 2019
Pale de Rase	Late Ordovician Calcshists	Reworked ore deposits	Quartz (Pb-Zn)	1-10	4	200-255			Cugeronne, 2019
Pale de Bideau	Late Ordovician Calcshists	Reworked ore deposits	Quartz (Pb-Zn)	5 - 16	15	185-320			Cugeronne, 2019
Les Argentieres	Lower Devonian dolomites closed to faulted contact with Mid-Devonian calcshists	Reworked ore deposits	Quartz (Pb-Zn)	25 -28	27	108-140			Munoz et al., 2015
Lacore	Lower Devonian dolomites closed to faulted contact with Mid-Devonian calcshists	Reworked ore deposits	Quartz (Pb-Zn)	18 -25	22	118-180			Munoz et al., 2015

1272 Table 2: List of geological occurrences and corresponding literature on fluid inclusions for
1273 diagenetic-hydrothermal cement related to syn-rift and syn-thrust events from the
1274 Pyrenees. Data on ore deposits the most probably affected by later hydrothermal processes
1275 of unknown age were also considered.

1276

1277

1278

1279

1280

1281